

AD-A102 074

PRATT AND WHITNEY AIRCRAFT GROUP WEST PALM BEACH FL 6--ETC F/6 11/6
REDUCTION OF STRATEGIC ELEMENTS IN TURBINE DISK ALLOYS.(U)

MAY 81 C C LAW, J S LIN, M J BLACKBURN

F49620-80-C-0048

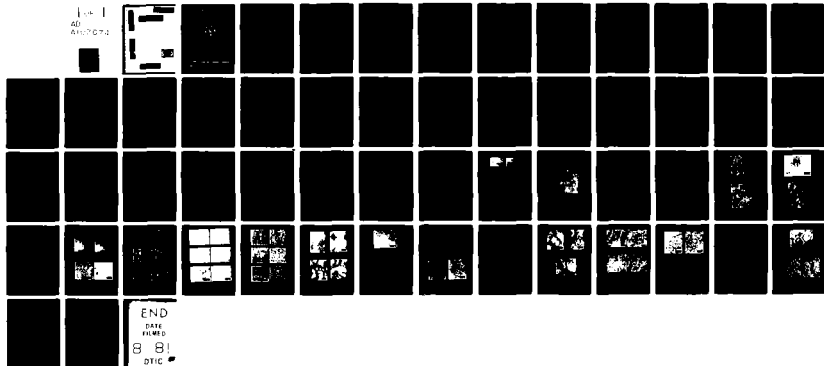
UNCLASSIFIED

PWA-FR-14913

AFOSR-TR-81-0554

NL

AD
A102074



END
DATE
FILMED
8 81
DTIC

AD A102074

DTIC FILE COPY

LEVEL

12

DTIC
ELECTE
S JUL 28 1981 D

FOSR-TR- 81 -0554

12

REDUCTION OF STRATEGIC ELEMENTS IN
TURBINE DISK ALLOYS

FINAL REPORT

March 1, 1980-February 28, 1981

UNITED STATES AIR FORCE OFFICE OF SCIENTIFIC RESEARCH
BUILDING 140
BOLLING AIR FORCE BASE, D.C. 20332



PREPARED BY:

C. C. LAW, L. S. LIN, AND M. J. BLACKBURN

MATERIALS ENGINEERING & RESEARCH LABORATORY

Accession For	
NTIS GRA&I	X
DTIC TAB	
Unannounced	
Justification	
By	
Distribution/	
Availability Codes	
Dist	Avail and/or Special
A	

S
JUL 28 1981
D

AIR FORCE OFFICE OF SCIENTIFIC RESEARCH (AFSC)
NOTICE OF TRANSMITTAL TO DDC
This technical report has been reviewed and is
approved for public release IAW AFR 190-12 (7b).
Distribution is unlimited.
A. D. BLOSE
Technical Information Officer

PRATT & WHITNEY AIRCRAFT GROUP

Government Products Division

P. O. Box 2691
West Palm Beach, Florida 33402



**UNITED
TECHNOLOGIES**

81 7 24 057

REF. NO. EII 81-200-7031-FR

Approved for public release;
distribution unlimited.



UNCLASSIFIED

SECURITY CLASSIFICATION OF THIS PAGE (When Data Entered)

18 REPORT DOCUMENTATION PAGE		READ INSTRUCTIONS BEFORE COMPLETING FORM
1. REPORT NUMBER AFOSR-TR-81-0554	2. GOVT ACCESSION NO. AD-702 074	3. RECIPIENT'S CATALOG NUMBER
4. TITLE (and Subtitle) Reduction of Strategic Elements in Turbine Disk Alloys		5. TYPE OF REPORT & PERIOD COVERED Final Report 3/1/80 - 2/28/81
7. AUTHOR(s) C. C. Law, J. S. Lin, and M. J. Blackburn		6. PERFORMING ORG. REPORT NUMBER -FR-14913
9. PERFORMING ORGANIZATION NAME AND ADDRESS United Technologies Corporation Pratt & Whitney Aircraft Group Government Products Div., W. Palm Beach, FL		8. CONTRACT OR GRANT NUMBER(s) F49620-80-C-0048
11. CONTROLLING OFFICE NAME AND ADDRESS Air Force Office of Scientific Research/NE Bolling Air Force Base D.C. 20332		10. PROGRAM ELEMENT, PROJECT, TASK AREA & WORK UNIT NUMBERS 61102F 16 2396/A1
14. MONITORING AGENCY NAME & ADDRESS (if different from Controlling Office) 1111 1 PT 4 Mar 82-21 F		12. REPORT DATE May 1981
		13. NUMBER OF PAGES 51
		15. SECURITY CLASS. (of this report) Unclassified
16. DISTRIBUTION STATEMENT (of this Report) APPROVED FOR PUBLIC RELEASE; DISTRIBUTION UNLIMITED		15a. DECLASSIFICATION/DOWNGRADING SCHEDULE
17. DISTRIBUTION STATEMENT (of the abstract entered in Block 20, if different from Report)		
18. SUPPLEMENTARY NOTES		
19. KEY WORDS (Continue on reverse side if necessary and identify by block number)		
20. ABSTRACT (Continue on reverse side if necessary and identify by block number) A study was conducted to characterize the effect of the substitution of nickel for cobalt in a modified IN100 alloy. The stacking fault energy of the austenitic matrix and the mechanical properties of both the matrix phase alloy and the superalloy were determined as a function of cobalt content. Among the mechanical properties evaluated - yield strength, creep, and low cycle fatigue, the effect of cobalt is most pronounced in creep. Substitution of nickel for all the cobalt (18%) in the alloy leads to a drastic reduction		

DD FORM 1473
1 JAN 73

EDITION OF 1 NOV 65 IS OBSOLETE

Unclassified

SECURITY CLASSIFICATION OF THIS PAGE (When Data Entered)

20. of creep rupture life and some decrease in ductility. However, intermediate levels of substitution (10%) have no adverse effect on creep properties. These results were confirmed in the AF115 alloy. Detailed studies of the microstructural and deformation characteristics of the alloys as a function of cobalt content revealed several important factors. Stacking fault energy, although low in all alloys, did vary sufficiently to lower creep resistance. In addition, the changes in precipitation processes for both the gamma prime and carbide phases also tended to degrade the creep capability.

Unclassified

TABLE OF CONTENTS

1.0	INTRODUCTION	1
2.0	EXPERIMENTAL	2
	2.1 Preparation and Testing of Single Phase Alloys	
	2.2 Preparation and Testing of MERL 76 and AF115	
3.0	RESULTS	5
	3.1 Single Phase Gamma Alloys	
	3.1.1 Stacking Fault Energy	
	3.1.2 Yield Strength and Strain Rate Sensitivity	
	3.1.3 Creep at 650-700°C	
	3.1.4 Creep at 760-810°C	
	3.2 Multi-Phase Alloys	
	3.2.1 Microstructures of MERL 76 and AF115	
	3.2.2 Creep of MERL 76 and AF115	
	3.2.3 Low Cycle Fatigue and Crack Propagation of MERL 76	
4.0	DISCUSSION	13
	4.1 Stacking Fault Energy of Single Phase Alloys	
	4.2 Mechanical Properties of Single Phase Alloys	
	4.3 Microstructures and Properties of MERL 76	
5.0	CONCLUSIONS	17
	REFERENCES	18
	ACKNOWLEDGEMENTS	20
	TABLES	21
	FIGURES	30

1.0 INTRODUCTION

Problems with the supply, delivery, and price of various raw materials are recorded on almost a daily basis in the technical and popular press. Although the energy situation appears more critical at the present time, means exist to satisfy power needs through the exploitation of fuels and systems that are not oil based. The same is not true in the case of other raw materials, especially metallic ores and metals in which reliance on external sources cannot be eliminated because of the lack of ore deposits within the USA. Table I lists some important metals, shows the percentage imported by the USA, and indicates the countries in which the greatest proven reserves are situated. It takes little imagination to visualize disruption in supply due to political instability or blackmail. Formation of cartels, similar to OPEC, cannot be ruled out in the future, but even without this, it is virtually certain that the cost of materials will continue to climb.

Advanced powerplants, such as gas turbine engines, are constructed of materials that consume large amounts of the metals listed in Table I. Thus, one must be concerned with the future availability and cost of materials used in critical defense systems. This potential problem has been recognized, and various steps have been proposed to eliminate or reduce the impact of the strategic element shortages. These approaches may be summarized as follows:

- Reduction of Input Material Requirements -- Current near net shape component programs seek to minimize material utilization through powder metallurgy, precision forging, and casting methods.
- Effective Recycling -- Scrap and other waste products are the subject of reclamation programs to improve utilization.
- Component Life Extension -- Programs are in place which seek to take full advantage of the capability of parts; for example, retirement for cause.
- Material Development -- Efforts to identify new alloys, based on readily available elements, are being actively pursued.

It is with this last approach that the program described in this proposal is concerned. Some of the larger components in a gas-turbine engine are the turbine disks which are made from nickel-base superalloys. Based on the engine cycle requirements, disk position, etc., the specific alloy is selected (within Pratt & Whitney Aircraft) from the alloys listed in Table II. Note that all these alloys consist, to a great extent, of elements listed in Table I, and large amounts are consumed in the production of disks. It may also be pointed out that these alloys are derived from earlier versions that were used for cast blades. The property requirements for disks are substantially different from those for turbine blades, and thus some changes in alloy chemistry may be tolerated while retaining the

required property balance.

The basic reasons for the attractive mechanical properties of nickel-base superalloys are reasonably well established. Essentially the precipitation of a large volume fraction of an ordered cubic phase ($L1_2$ type) that closely matches the face-centered, nickel-rich solid solution matrix is required. Such a structure is created by the addition of aluminum and titanium to form the $Ni_3(Al, Ti)$ phase.

However, other elements are also added to impart other desirable characteristics to the alloy; for example, chromium for oxidation-corrosion resistance, molybdenum to strengthen the matrix, etc. Cobalt appears to play several important roles in mechanical properties. Previous studies of nickel-cobalt alloys(1-3) and Nimonic alloys (4) have revealed that cobalt decreases the stacking fault energy of nickel and the solid solubility of aluminum, titanium, and carbon. Recent studies on Waspaloy with different cobalt concentrations(5) show mechanical property changes, particularly in creep, consistent with these conclusions. However, a detailed microstructure-property correlation has not been carried out in these previous investigations. The objectives of this study are, therefore, to determine the microstructural and deformation behavior in nickel-base superalloys with various cobalt contents, to relate changes to measured mechanical properties of the alloys, and thus identify directions for future alloy development.

In nickel-base superalloys cobalt partitions primarily to the nickel-rich solid solution matrix, gamma phase. It is considered that a basic understanding of cobalt effects in the gamma phase is a prerequisite to gaining insight into the mechanical behavior of the more complex, multi-phase superalloys. Further, determination of stacking fault energy in the single phase gamma alloy is considerably simpler than in the superalloys. Therefore, a preliminary study was undertaken which involved preparation of gamma phase alloys with the same composition as the matrix phase in MERL 76, one of the two superalloys selected in this study. The cobalt contents of the gamma phase alloys were varied from 0% to the value determined in the matrix of MERL 76, 30 wt.%. Results from this preliminary study are coupled with a subsequent study involving microstructure and mechanical property characterizations of MERL 76 and AF115 to provide a detailed evaluation of cobalt effects. The mechanical properties studied are creep, strain-controlled low cycle fatigue, and fatigue crack propagation.

2.0 EXPERIMENTAL

2.1 Preparation and Testing of Gamma Alloys

The composition of the matrix phase in MERL 76 was computed from the analyzed alloy composition and the composition of the extracted gamma prime phase, obtained by anodic dissolution of the gamma phase using the procedure described by Kriege and Baris(1). In the computation, gamma prime volume fractions of 54 weight percent and 60 volume percent were used. These values were obtained by gravimetric technique and by image analysis of optical and electron replica micrographs, respectively. The computed matrix compositions of MERL 76 are given in Table III on which the compositions of the gamma alloys were based, except that the Al and Ti concentrations were reduced to suppress precipitation of gamma prime phase. Gamma alloys with four levels of Co were prepared nominally at 30, 15, 5, and 0 weight percent; the concentrations of other elements were unchanged. Alloys were produced by arc melting and casting into 6.4 mm diameter rods in a water-cooled copper mold. The analyzed compositions are given in Table IV and the alloys numbered 29 to 32. The rods were hot isostatically pressed at 1195°C for 3h to close casting porosity and then heat treated for 8h at 760°C. No $\text{Ni}_3(\text{Al},\text{Ti})$ precipitates were found after the heat treatment. The grain sizes are 0.15, 0.12, 0.35, and 0.34 mm for Alloys 29, 30, 31, and 32, respectively.

Specimens of the heat treated alloys were deformed in compression to small strains ($\sim 2 \times 10^{-3}$) at 20°C to determine features of the dislocation substructures. Thin foils for electron microscopy were taken normal to the compression axis and electropolished according to established procedure (2). Dislocations tended to be confined to the octahedral slip planes, and separation of unit dislocations into partials could be detected. Stacking fault energy was calculated from measurements of equilibrium separations of Shockley partials which were imaged using weak beam dark field \bar{g} ($3\bar{g}$) technique(3-5). \bar{g} vector of $0\bar{2}2$ type was used for imaging. A theoretical consideration of the measurement of the separation of dissociated glide dislocations in Ni using the weak beam technique has been presented by Carter and Holmes(6). Measurements were made only from partials on octahedral slip planes which are within $\pm 15^\circ$ from the foil surface. Several measurements were taken along a stacking fault ribbon, and the average was used for the calculation of stacking fault energy.

Mechanical tests conducted on cylindrical specimens of these alloys included yield strength and strain rate sensitivity measurements at temperatures up to 800°C, creep tests at temperatures between 650°C and 810°C. All tests were in compression and performed in air. Strain was measured by a linear voltage differential transformer (LVDT) attached to the alumina compression platens.

2.2 Preparation and Testing of MERL 76 and AF115

Prealloyed ingots with compositions based on MERL 76, containing 10 and 0% cobalt, and AF115, containing 10 and 0% Co, were vacuum induction melted and atomized in an experimental unit. All the powders were

screened to -80 mesh fraction. A standard 18% cobalt MERL 76 was obtained from a large production heat screened to -325 mesh fraction. The powder of each alloy was outgassed at 260°C and transferred to a preevacuated stainless steel container which, after sealing, was then consolidated by hot isostatic pressing. The consolidated materials were solution heat treated and aged at 760°C for 8h followed by air cooling. The powder consolidation and solution treatment temperatures were below the γ' solvus of the alloy by about 10°C to 20°C in most cases. Details are given in Table V. The analyzed compositions of the alloys are given in Table VI.

Tensile creep-rupture testing was performed in air under constant loads at 704°C. Creep strains were continuously recorded from an extensometer fixed to the test specimens. The gage section of the tensile creep specimens is 2.5 mm diameter, 20.3 mm long. Compressive creep test techniques, similar to those used for the gamma alloys, were also employed to obtain creep data at various temperatures. Strain-controlled low cycle fatigue tests were performed in air at 480°C and 650°C at a total strain range 0.014, minimum to maximum strain ratio of -1.0, 10 cycles per minute, using a servo-hydraulic machine. The fatigue specimens were similar to those used by Wells and Sullivan(7). Stress-controlled fatigue crack propagation rates were measured at 650°C using center-notched sheet specimens. The specimen design and calculation of the stress intensity factor is given by Tada et al(8). Prior to the crack growth measurements, starting cracks were introduced at the ends of the center notch by high frequency low amplitude alternating stresses at 20°C. The crack growth was measured at a minimum to maximum stress ratio of 0.1 at 60 cycles per minute.

3.0 RESULTS

3.1 Single Phase Gamma Alloys

3.1.1 Stacking Fault Energy

Typical weak beam images of the partial dislocations are shown in Figure 1. The average equilibrium separations of the Shockley partials in the gamma alloys with various Co contents are given in Table VII. For an isotropic material, the stacking fault energy γ is related to the equilibrium separation of the partials, Δ , by the expression (9):

$$\gamma = \frac{Gb_1b_2}{8\pi\Delta} \left(\frac{2-\nu}{1-\nu} \right) \left(1 - \frac{2\nu \cos 2\alpha}{2-\nu} \right) \quad (1)$$

where G is the shear modulus, ν is the Poisson's ratio, α is the angle between the total Burgers vector b , and the dislocation line, b_1 and b_2 , are the Burgers vectors of the two partials. For anisotropic material with cubic lattice, the corresponding relationship is (10)

$$\gamma = \frac{b_1b_2}{8\pi\Delta} \left[k_s (1 + 2 \cos 2\alpha) + k_e (1 - 2 \cos 2\alpha) \right] \quad (2)$$

where

$$k_s = \left[\frac{C_{44}}{2} (C_{11} - C_{12}) \right]^{1/2}$$

$$k_e = (C_{11} + C_{12}) \left[\frac{C_{44}(C_{11} - C_{12})}{C_{11}(C_{11} + C_{12} + 2C_{44})} \right]^{1/2}$$

The C_{11} , C_{12} , and C_{44} are elastic constants which, in Ni-Co binary alloys, can be expressed as (11)

$$C_{ij}(c) = C_{ij}(\text{Ni}) \left[1 + 8.54 \times 10^{-4} c \right] \quad (3)$$

where c is the concentration of cobalt in atomic percent, $C_{ij}(\text{Ni})$ are the elastic constants for pure nickel.

The computed stacking fault energies of the gamma alloys are given in Table VII, which show that the γ of the gamma alloys decreases rather slowly with increasing cobalt content. Relative to the γ of Alloy 32 (0% Co), addition of 30% Co (Alloy 29) reduces the γ by a factor of 2. Further, the γ calculated by equation (2), is about 20 percent lower than those calculated by equation (1), a difference which is small

compared with other sources of error in determining the stacking fault energy(12) and, therefore, the differentiation of these two sets of values is inconsequential. However, to avoid confusion, the stacking fault energy referred to in all subsequent discussions are those calculated using Eq. 1.

3.1.2 Yield Strength and Strain Rate Sensitivity

The yield strengths of the gamma alloys with 30 wt.% cobalt (Alloy 29) and 0 wt.% cobalt (Alloy 32) at several temperatures are shown in Figure 2. Alloy 29 generally has higher yield strengths than Alloy 32, but the differences become smaller as the temperature increases. At temperatures around 700°C, the yield strength curve of Alloy 29 exhibits a small peak which is not found in Alloy 32. The shape of the yield strength peak can be changed by aging treatment, e.g. after a 90-hour age at a test temperature of 677°C the yield strength of Alloy 29 increases to 260 MPa from 144 MPa; essentially no change was observed in Alloy 32 after aging.

The strength increase in Alloy 29 was due to the precipitation of very fine γ' particles which, although not detected by electron microscopy in the samples yielded at 700°C, but could be observed readily after prolonged aging at temperatures around 700°C. Precipitation of γ' particles after similar aging was scarcely detectable in Alloy 30 (17% Co) and not found in Alloys 31 (7.6% Co) or 32 (0% Co).

Transmission electron microscopy on specimens deformed at 20°C and 704°C showed no significant difference in dislocation structures between Alloys 29 and 32. In both alloys, deformation was by heterogeneous planar slip involving formation of dipoles and multipoles in an early stage of deformation. With increasing strain at 704°C, tangled arrays start to form. There was more evidence of cross-slip activity in Alloy 32 than in Alloy 29, leading to a slightly more dispersed dislocation structure in Alloy 32 as shown in Figure 3.

The plastic flow behavior of Alloy 29 at two different strain rates and various temperatures is illustrated in Fig. 4. Two interesting phenomena occur at temperatures around 600°C, jerky flow and negative strain rate sensitivity. The characteristics appear to be independent of alloy composition, and the dependence on temperature, strain rate, and strain is similar to the jerky flow and strain rate sensitivity behavior in INCONEL 600 (15.9 at.% Cr - 10.1 at.% Fe - 0.4 at.% C - bal. Ni) described most recently by Mulford and Kocks (13). The strain rate sensitivity, defined here as $(\Delta \ln \sigma / \Delta \ln \dot{\epsilon})_T$ and determined at strains slightly above the yield, is plotted as a function of temperature for Alloys 29 and 32 in Figure 5, which illustrates that there are no significant differences between the two alloys.

3.1.3 Creep at 650°C - 700°C

Initial survey of creep behavior of the gamma alloys was conducted at temperatures between 650°C and 704°C. At stresses slightly below the

yield strength, the creep rates were found to be extremely slow and appeared to be insensitive to small changes in both temperature and stress. For example, at 650°C and under a stress of 80% of the yield strength, a creep rate of $4 \times 10^{-6} \text{ h}^{-1}$ was measured on Alloy 30 (17 wt.% Co), essentially the same creep rate was measured at a higher temperature 677°C. In order to obtain measurable differences between these alloys within a reasonable period of time, the stress or the temperature was subsequently increased. Table VIII shows the minimum creep rates of the gamma alloys at 704°C at stresses 120% of their respective yield strengths. Compared with Alloy 32 (0% Co), the creep rates of Alloys 29 (30% Co), 30 (17% Co), and 31 (8% Co) are 22.3, 3.2, and 2.7 times slower, respectively. The relatively large difference in creep resistance between Alloys 29 and 32 cannot be attributed entirely to stacking fault energy, which varies linearly with Co content. Part of this difference is associated with the dynamic precipitation of fine γ' particles in Alloy 29, as shown below.

Transmission micrographs of specimens of Alloys 29 and 32 creep tested at 704°C are shown in Figures 6 and 7, respectively. The dislocation distribution in Alloy 32 is rather homogeneous, revealing no areas of concentrated slip, but the dislocation structure in Alloy 29 consists of clusters confined to active slip systems. Some cross-slip activity in Alloy 29 is also evident. Another significant difference between Alloys 29 and 32, which can be observed in Figures 8 and 9, is the formation of a fine γ' precipitate during creep of Alloy 29 but not in Alloy 32. These particles, which have an average size of about 10nm after testing for 66h at 704°C, are shown in dark field in Figure 8, which includes the corresponding diffraction pattern showing well defined superlattice reflections. These particles clearly impede dislocation motion as evidenced by the formation of dislocation loops, Figure 9.

3.1.4 Creep at 760°C - 810°C

The effect of stacking fault energy on creep should be more evident at these temperatures where creep behavior is not complicated by dynamic precipitation of γ' particles and by the negative strain rate sensitivity phenomenon. In this regime, creep rate ($\dot{\epsilon}$) can be empirically related to the stacking fault energy (γ), applied stress (σ), modulus (E), and diffusivity (D) by (14):

$$\dot{\epsilon} = AD^{-m} \left(\frac{\sigma}{E} \right)^n \quad (14)$$

where A, m, and n are constants. The value of n was determined to be 4.9 for Alloys 29 and 32. To determine m, creep tests of the gamma alloys were performed at 802°C under a constant (σ/E) value of 5.3×10^{-6} . The elastic moduli were calculated using the Ni-Co binary alloy data of Pfaff (11). Results are plotted as $\ln(\dot{\epsilon}/D)$ versus $\ln \gamma$ in Figure 10. The diffusivities for the gamma alloys are not known but are considered here to be proportional to the tracer diffusion coefficients of Co in Ni-Co binary alloys, data of which are available(15). From Figure 10, m is determined to be about 2.0.

The difference in creep resistance between Alloys 29, 30, and 32 over this temperature range is smaller than that at the lower temperature range, and the difference decreases with increasing temperature, Figure 11. The apparent creep activation energies calculated from the slopes of the ϵ vs $1/T$ curves in Figure 11 are 457, 345, and 272 KJ mol⁻¹ for Alloys 29, 30, and 32, respectively. For comparison, the activation energy for self-diffusion in nickel is 276 KJ mol⁻¹, which is quite close to the apparent activation energy for creep in Alloy 32. The larger creep activation energy and creep resistance of the higher cobalt alloy are considered to be due to the presence of higher internal stress resulting from a higher dislocation density. Indeed, the dislocation density in Alloy 29, after creep at 800°C, is 4 times higher than that in Alloy 32, Figure 12. The increase in dislocation density with cobalt content can be related to the decrease in kinetics of dislocation recovery mechanisms with decreasing stacking fault energy.

3.2 Multi-Phase Alloys

3.2.1 Microstructures of MERL 76 and AF115

The as-atomized powders were checked for possible contamination using a cathodoluminescence technique(16) in which the presence of very thin ceramic oxides on powder particle surfaces can be detected by the preferential emission of electromagnetic radiation in the visible spectral regions. Some of the results are illustrated in Figure 13 for the 10% Co AF115. Figure 13a shows the secondary electron image of the powder particles. The cathodoluminescence image at the same location is shown in Figure 13b from which several oxide covered powder particles can be observed. The oxide is rich in Hf. It was found that all powders made in the experimental unit showed this form of contamination to a various degree. The oxide coverage was the largest in the 10% Co AF115 and smallest in the 0% Co AF115. Standard MERL 76 (18% Co) alloy taken from a production run showed no evidence of oxide coverage on particles surfaces. As will be shown, the presence of the oxide-covered powder particles appears to have little effect on creep rupture properties but seriously degrades fatigue life.

The microstructures of MERL 76 and AF115 alloys as a function of cobalt content are shown in Figures 14, 15, and 16 from which some differences in γ' particle size and morphology can be observed. In the MERL 76 base alloys, the primary γ' particle size is the largest in the 10% Co alloy and the smallest in the 18% Co alloy. There are more primary γ' particles in the 0% Co MERL 76 than in the other alloys. The sizes of the secondary γ' particles in the 18% Co MERL 76 and 10% Co MERL 76 are about the same and are smaller than those in the 0% Co MERL 76. Equivalent differences are not observed in the AF115 base alloys, Figure 16. Therefore, the variation in the MERL 76 base alloys cannot be unambiguously attributed to the effect of cobalt alone. The grain sizes are ASTM No. 10, 8, 9 for the 18%, 10%, and 0% Co MERL 76 alloys, respectively, and are ASTM No. 10, 9, 9 for the 15%, 10%, and 0% Co AF115 alloys, respectively. These differences could be changed by using different processing

temperatures. The total γ' volume fraction in the MERL 76 base alloys are about the same, ~ 0.6 , independent of Co content. Gamma prime solvi increase with decreasing cobalt content and were determined to be 1191°C, 1207°C, 1218°C, and $> 1238^\circ\text{C}$ for the 18%, 10%, 5%, and 0% Co MERL 76 alloys(17). Some other effects of cobalt can be observed in transmission electron microscopy of thin foils. Figure 17 shows the presence of very fine γ' particles between the secondary γ' particles in the 18% Co MERL 76 after heat treatment. The precipitation of such particles occurred to a much lesser extent in the 0% Co MERL 76. This difference may be attributed to the lower solubility of Al and Ti in the γ phase with increasing Co content at lower temperatures, as observed in Nimonic alloys(18). Although the amount of the fine γ' particles precipitated in the high cobalt alloys are small, it has an appreciable effect on creep and yield strength as demonstrated in the gamma alloy.

Another important effect of Co can be observed in Figure 18, which shows more carbide particles precipitated at grain boundaries of the 0% Co MERL 76 than in the 18% Co MERL 76. The carbides in the 18% Co MERL 76 are predominantly MC type, rich in either Hf or Ti. In contrast, the 0% Co MERL 76 contains, in addition to MC carbides, a considerable amount of $M_{23}C_6$ type carbides rich in Cr and Mo. As will be shown later, $M_{23}C_6$ type of carbide also precipitate intragranularly during creep of the 0% Co MERL at intermediate temperatures. The enhanced precipitation of carbides in the 0% Co MERL 76 is also consistent with previous observation in Nimonic alloys(18). An interesting observation, which may be associated with the precipitation of $M_{23}C_6$ type carbide, as discussed later, is the presence of fringe contrast at the γ/γ' interface in the 0% Co MERL 76 (Figure 19) but not in the 18% Co MERL 76. Since the fringe contrast arises from the coherent strain at the γ/γ' interface, its occurrence in the 0% Co MERL 76 implies a larger γ/γ' lattice misfit than in the case of the 18% Co MERL 76. A reason for this misfit will be discussed later.

3.2.2 Creep of MERL 76 and AF115

Some of the creep-rupture results of MERL 76 base alloys, containing 0%, 10%, and 18% Co, are given in Table IX, from which it can be seen that the rupture life and ductility of the 10% and 18% are rather similar. However, both the rupture life and ductility, especially reduction in the area of the 0% Co MERL 76, are considerably lower. AF115 exhibits similar deficiencies in creep-rupture properties when nickel is substituted for all the cobalt, Table X. The creep rupture properties of the 10% Co AF115 are slightly inferior to the 15% Co AF115 especially at low stresses. A change in creep-rupture properties with cobalt content is also evident from the stress dependence of the creep rate and rupture life given in Figures 20 and 21. Within the limited stress range used for the testing, the creep rate and rupture life of both the 0% Co MERL 76 and the 18% Co MERL 76 can be approximated by a power law. Interesting differences in the slopes or the stress exponent of the power law can be observed from Figures 20 and 21. The stress dependence of creep rate and rupture life of the 18% Co MERL 76 are unequal with exponents of 14 and 5 respectively; whereas the stress exponents of the 0% Co MERL 76 are about the same with values of 7. The fracture of the 18% Co MERL 76 was associated with a large component

of grain boundary sliding contribution(19), Figure 22a. In contrast, the fracture of the 0% Co MERL 76 appears to be similar to that of AF115 and the modified MAR-M432 examined previously(19) and is attributed to cavitation at grain boundary particles, Figure 22b.

To determine the effect of cobalt on creep at various temperatures, compressive creep tests were performed on the 18% Co MERL 76 and 0% Co MERL 76 at a series of temperatures under constant stress. The temperature was sequentially increased in 28°C increments from an initial temperature of 650°C. A relatively large stress 860 MPa was chosen so that creep rate could be measured within a reasonable period of time at the lowest temperature. The temperature was increased whenever the creep rate appeared to be constant. However, this presented a problem at high temperatures in which, because of the large applied stress, the creep rate increased continuously. In these cases the average creep rate in 0.5 h to 2 h was measured. Results are illustrated in Figure 23 from which two temperature regimes can be discerned based on temperature dependence of creep rate and in the magnitude of the creep rate between the two alloys. At intermediate temperatures ($\sim 680^\circ\text{C}$), the creep rates of the 0% Co MERL 76 are larger than those of the 18% Co MERL 76 by a factor slightly over 10. At higher temperatures ($>720^\circ\text{C}$), the difference is lower, a factor slightly less than 10. As suggested by the gamma alloy results, the larger difference at intermediate temperatures can be associated with precipitation of fine gamma prime particles during creep. Supporting evidence for such precipitation can be seen in Figure 24, which shows a considerable increase and some coarsening of the fine gamma prime particles after creep test for 130 h at 675°C , compared with the as-heat-treated material. Concomitant changes in creep rate could be expected due to such precipitation and were observed, as illustrated in Figure 25. The creep rates of the 18% Co MERL 76 decrease continuously, while those of the 0% Co remain constant after 40 h of test. Another interesting observation of creep at 675°C was that very thin carbide platelets of dimensions $0.2\ \mu\text{m}$ were precipitated intragranularly in the 0% Co MERL 76, Figure 26. These carbides are rich in Cr and Mo. Formation of such carbides was not detected in the 18% Co MERL 76.

The slight increase in the temperature dependence of the creep rate at higher temperatures, Figure 23, could be associated with a number of causes including coarsening of γ' particles and the absence of the negative strain rate sensitivity phenomenon as suggested by the gamma alloy results.

The creep deformation structures of the 18% Co and 0% Co MERL 76 at 704°C and 815°C are shown in Figures 27 and 28, respectively. At the lower temperature, creep deformation in the 18% Co alloy involved formation of a large number of microtwins which are absent in the 0% Co alloy, although short stacking fault segments are observed in the 0% Co alloy. The higher dislocation density in the 0% Co MERL 76 is probably due to the higher creep strain compared with the 18% Co MERL 76. After creep at 815°C , microtwins could no longer be observed in the 18% Co alloy; instead short stacking fault segments confined to γ' particles are seen. No stacking fault segments were observed in the 0% Co alloy after creep at 815°C .

The dislocation densities in both alloys are considerably lower than those resulting from creep at the lower temperature. In Figure 28b, the fringe contrast at the γ/γ' interface arises from the γ/γ' coherency strain.

3.2.3 Low Cycle Fatigue and Crack Propagation of MERL 76

The fracture lives of the MERL 76 base alloys, tested at a strain range of 0.014 at 480°C and 650°C, are given in Table XI, from which there appears to be a correlation of life with cobalt content. The fracture life increases with increasing cobalt content at both temperatures. It should, however, be pointed out that the magnitude of the life difference cannot be solely attributed to the effect of cobalt. The relatively low lives of the 0% Co and 10% Co alloys are partially due to the fact that some of the powder particles in the low cobalt alloys were oxidized. It was also found that inclusion size and content played an important role in determining the fracture life. In fact, the fractures of the low cobalt alloys were initiated at oxide inclusions which were not detected at the fracture origins of the 18.0% Co MERL 76, reflecting the finer mesh size and general higher quality of the heat used. For a given alloy, the appearances of the fatigue fracture at both temperatures are similar. Those at 650°C are shown in Figure 29, from which it can be seen that the fractures are transgranular for the 18% Co MERL 76 and intergranular for the 0% Co MERL 76, while the 10% Co alloy exhibited a mixed failure mode. The smooth facets in Figure 29b are the surfaces of large primary γ' particles located at grain boundaries. The change in fracture mode may be associated with the larger amount of grain boundary carbides when the cobalt level is reduced. Testing of the 10% Co AF115 at a lower strain range (0.013) and temperature (20°C) lead to a fracture life of 170 cycles and the fracture occurred along prior particle boundaries. This premature failure is, no doubt, the result of powder contamination as revealed by the cathodoluminescence technique. Therefore, testing of the AF115 alloys was suspended.

The stress range versus cycle curves for the MERL 76 base alloys at 480°C are presented in Figure 30. All three alloys cyclically harden up to the point of fracture at this temperature. There is essentially no difference in the rate of hardening between these alloys. The cyclic response of the 0% Co MERL 76, including the shape and areas of the hysteresis loops, is almost identical to that of the 18% Co MERL 76. However, the stress range for the 10% Co MERL 76 is slightly lower at both 480°C and 650°C. The cyclic behavior of the three alloys at 650°C is similar to that at 480°C, except that the alloys hardened at lower rates and reached a plateau at about 0.5 fracture life beyond which softening occurred, Figure 31.

No discernible difference was observed in the fatigue dislocation structures between the 0% Co MERL 76 and 18% Co MERL 76. In an early stage of fatigue deformation, dislocations are arrested at the γ/γ' interface, Figure 32. After fracture, very high dislocation densities in the matrix phase can be observed, Figure 33.

The data for fatigue crack growth at 650°C are given in Figure 34. At the test condition used ($R = 0.1$, 60 cycles per minute), no important differences in crack growth rates were observed between the MERL 76 base alloys with 0%, 10%, and 18% Co.

4.0 DISCUSSION

4.1 Stacking Fault Energy of Single Phase Alloys

It is interesting to compare in Figure 35 the effect of Co in the gamma alloys with that in the Ni-Co binary alloys. It is obvious that the rate of change of stacking fault energy with Co is over three times faster in the Ni-Co binary alloys than in the gamma alloys. The fact that Co has a different influence on stacking fault energy in more complex alloys may not be surprising. Stacking fault energy is related to the difference of cohesive energy between fcc and hcp lattices. Cohesion in the present case is mainly governed by the bonding energy of the d electrons, which is related to the density of states of the d band and the Fermi level(21). Alloying modifies both the density of states of the d band and the Fermi level in a complex way which depends not only on the characteristic of the alloy element to be added but also on the current electronic state of the host lattice. It may therefore be inferred that addition of Co to pure Ni should have a different effect than addition of Co to a Ni solution, which contains a large quantity of other elements, as in our gamma alloys.

The above consideration and our data suggest that, in general, one cannot compute the stacking fault energy of a multi-element concentrated solid solution using data from binary alloys. However, it may still be useful to estimate the stacking fault energy of a multi-element solid solution using binary alloy data. Beeston and France(22) suggested that the stacking fault energy of a multi-element solid solution $(\bar{\tau}/Gb)_v$ can be approximated by

$$(\bar{\tau}/Gb)_v = (\bar{\tau}/Gb)_{Ni} (1 - 2.0Cr - 1.8 Al - 5.83 Ti - 1.12 Co - 4.3 Mo) \quad (5)$$

where $(\bar{\tau}/Gb)_{Ni}$ is the stacking fault energy for Ni which is 5.3×10^{-3} (2) and Cr, Al, Ti, Co, and Mo in Equation (5) are concentrations in atomic fractions of the respective elements in the solid solution. Results of our calculation are indicated by Curve C in Figure 35, which predict a hcp lattice for Alloy 29 (negative stacking fault energy), contrary to our observation. Another problem with Equation (5) is its linear approach, which ignores interaction of alloying elements and, therefore, predicts alloying effects identical to that in the binary alloy, contrary to our results on gamma alloys. A better approximation to the stacking fault energy of a multi-element solution appears to have the following form:

$$(\bar{\tau}/Gb)_v = (\bar{\tau}/Gb)_{Ni} \exp - \sum_{i=1}^n A_i X_i \quad (6)$$

where X_i is the atomic percent of element, i and A_i is the slope of \log (stacking fault energy) vs $\log X_i$ for element i in the Ni binary alloy. Values for A_i are given in Table XII. The stacking fault energies calculated from Equation (6) for the alloys in the present study and those examined by

Oblak (23) are given in Table XIII. Good agreement between the calculated values and the experimental data can be seen.

4.2 Mechanical Properties of Single Phase Alloys

The study of gamma alloys reveals three salient features which have important implications in understanding the effect of cobalt on mechanical properties of nickel-base superalloys.

1. The stacking fault energies of the matrix phase in nickel-base superalloys are rather low and change by a factor of two for a variation of 30% in cobalt content.
2. Cobalt reduces the solubility of Al and Ti in nickel solid solutions at lower temperatures. This change is reflected in the precipitation of very fine gamma prime particles at temperatures about 700°C in cobalt rich alloys.
3. Occurrence of negative strain rate sensitivity at temperatures around 600°C, which is independent of cobalt content.

The low stacking fault energy of the superalloy matrix ($\tau/Gb = 1 \text{ to } 2 \times 10^{-3}$) means that the heterogeneous planar slip characteristics of the superalloys at intermediate temperatures will not be changed in a major way by variation of cobalt content. Therefore, "short-time" mechanical properties, which are dependent on the slip characteristics, should not be markedly changed by cobalt level. This expectation has indeed been demonstrated in the yield strength behavior of the gamma alloys and is confirmed by the insensitivity of fatigue response and fatigue crack propagation rates of the MERL 76 base alloys. However, time dependent elevated temperature properties, such as creep and fatigue under dwell cycles, which are influenced significantly by the kinetics of dislocation recovery mechanisms, should be affected by cobalt level. In this case stacking fault energy determines the ease with which partial dislocations can constrict and be dispersed by cross-slip or climb processes. At temperatures above 760°C, the creep resistance of the gamma alloys should be proportional to the stacking fault energy to the power of about 2 from Equation (4). Thus, Alloy 29 (30% Co) creeps at a rate about four times slower than Alloy 32 (0% Co). Quantitative extension of the gamma alloys results to MERL 76 alloys requires a suitable model for a multiphase system which is not available at present; however, it is interesting to note that exactly the same order-of-magnitude difference is observed between 18% Co MERL 76 and 0% Co MERL 76.

At temperatures below 760°C, cobalt has another beneficial effect, which is directly related to previous observations that cobalt lowers the solubility of Al and Ti in nickel solid solutions and results in a slightly larger volume fraction of γ' phase (18,24). However, in our study, the additional γ' precipitation occurs during aging or testing at temperatures below 760°C. These γ' particles are very fine and have a measurable effect on the yield strength and creep of the gamma alloys. The precipitation of the fine γ' particles was also detected in the 18% Co MERL 76, and such precipitation,

or perhaps the precursor-state of short range ordered regions (25), again, has an appreciable effect on the creep of MERL 76.

The occurrence of the negative strain rate sensitivity and the associated jerky flow behavior in the gamma alloys is interesting from practical and theoretical points of view. As also observed in other alloy systems (26, 27), the negative strain rate sensitivity phenomenon contributes toward unusual creep behavior as well as imparts high creep resistance. In the case of multi-element nickel solid solutions, the negative strain rate sensitivity was attributed either to formation of Ni_3Cr type short-range ordered regions (28) or to dynamic strain aging involving Cr (13). In the gamma alloys, other as yet unidentified elements must also contribute to the negative strain rate sensitivity since elimination of Cr reduced the magnitude of the negative strain rate sensitivity but did not completely suppress it (29). The role of the matrix negative strain rate sensitivity on the creep resistance of the two phase alloys is not clear. It is further complicated by the fact that the two phase alloys did not exhibit negative strain rate sensitivity (29). However, for a more realistic theoretical treatment of the two-phase alloys, the negative strain rate sensitivity should be taken into consideration instead of assuming a simple nickel solid solution behavior, as was done previously (30).

4.3 Microstructures and Properties of MERL 76

As may be expected, the effect of cobalt on microstructure and properties of two phase alloys is more complicated than in the case of the gamma alloys. An additional effect, which must be taken into consideration, is the decrease of solubility of C in the matrix phase with reduction of the Co level, which results in the formation of more carbide particles of $M_{23}C_6$ type at intermediate temperatures. The present observation is consistent with those in Nimonic alloys (18), Waspaloy (24), and cast MERL 76 (29). The predominant type of carbide in the 18% Co alloy is MC, which precipitate as cuboidal and equiaxed particles distributed intra- and intergranularly. The MC particles are rich in either Hf or Ti. In the 0% Co alloy besides the MC type carbides, $M_{23}C_6$ type carbides are also precipitated at grain boundaries after aging treatment at 760°C. The $M_{23}C_6$ particles are rich in Cr and Mo.

The presence of the additional carbide particles at grain boundaries in the 0% Co alloy changes the fracture behavior. In fatigue the 18% Co alloy fractured transgranularly, while the 0% Co alloy fractured intergranularly with a life about six times lower than that of the 18% Co alloy. These observations are consistent with those in the Ni-Co binary alloys (31). However, the magnitude of the life difference in the present case is considered to be attributable, to a large extent, to the presence of contaminated powder particles in the low cobalt alloys. The observations that both the 18% Co and 0% Co alloys exhibit identical cyclic hardening and damping behavior also suggest a smaller life difference if the powders were of the same cleanliness.

In the case of the binary alloys, Ni-67% Co and Ni-55% Co, which have stacking fault energies of 15 and 45 mJm^{-2} , respectively, a three-fold decrease in fatigue life at room temperature was observed in the high stacking fault energy alloy. The life difference in the binary alloys was shown to be associated with a change in crack initiation behavior. Cracks initiated at twin boundaries in the low stacking fault energy alloy and at grain boundaries in the high stacking fault energy alloy. The stacking fault energies of the 18% Co MERL 76 and 0% Co MERL 76 are 19 and 38 mJm^{-2} , respectively, which fall between those of the Ni-Co binary alloys. Possibly because of the difference in test temperatures, twinning was not observed in the present alloys, which were deformed at 650°C but was observed in U700 (calculated stacking fault energy 23.4 mJm^{-2}) after fatigue deformation at room temperature (7). Instead, high densities of dislocations, distributed uniformly in the matrix phase, were observed in the present alloys. The uniform dislocation distribution is related to the activation of a large number of dislocation sources rather than to stacking fault energy effect. It is likely that in the present alloys part of the life difference can also be related to the crack initiation stage as no important difference in crack propagation rates was observed.

The grain boundary M_{23}C_6 carbide particles in the 0% Co alloy also reduced the creep rupture ductility and modified the fracture mode as evidenced by changes in the fractographic features and stress dependence of rupture life. More carbide particles were precipitated at grain boundaries and intragranularly as very thin platelets during creep of the 0% Co alloy at temperatures at least as low as 650°C. There are at least two indirect effects associated with precipitation of the M_{23}C_6 type carbides in the 0% Co MERL 76. Removal of Cr and Mo from the matrix increases the stacking fault energy(22) and decreases the lattice parameter of the matrix phase(32). Since the lattice parameter of the γ' phase in the 18% MERL 76 is larger than that of the γ phase, reduction of Cr and Mo in the γ matrix through formations of M_{23}C_6 carbide further increases the γ/γ' lattice misfit. The increase in the coherency strain in the 0% Co MERL 76 is manifested by the fringe contrast at the γ/γ' interface. Lattice mismatch has been considered to be beneficial for creep resistance at temperatures where γ' coarsening is unimportant (19). Thus, reduction of Co content need not necessarily degrade the creep resistance, for this could be a positive effect. A similar situation is encountered for solid solution effects, a decrease of Co level increases the amount of Al and Ti in the nickel solution matrix phase and, therefore, decreases the stacking fault energy of the matrix phase, which should improve creep resistance.

The effects of cobalt on microstructure and creep capability of MERL 76 are summarized in Table XIV. Since cobalt has both positive and negative effects on creep, any changes in alloy composition to increase creep resistance at a given cobalt level must be approached with care.

5.0 CONCLUSIONS

The major conclusions that can be drawn from the results of this study are as follows:

1. Among the mechanical properties evaluated - yield strength, creep, and low cycle fatigue the effect of cobalt was found to be most pronounced in creep.
2. Reduction of cobalt contents from the standard compositions, 18% in MERL 76 and 15 % in AF115, to 10% have no adverse effect on creep properties. Drastic reduction of creep properties, especially rupture life, in both alloys was observed when all the cobalt was substituted with nickel.
3. The microstructural effects and consequences in creep properties due to a reduction of cobalt content in MERL 76 were found to be:
 - a. an increase in stacking fault energy which leads to faster dislocation recovery processes and lower creep resistance.
 - b. an increase in solubility of aluminum and titanium in the austenitic matrix which leads to smaller amounts of fine gamma prime particles and lower creep resistance.
 - c. a decrease in solubility of carbon in the austenitic matrix which results in precipitation of more $M_{23}C_6$ type carbide particles at grain boundaries and lower creep rupture ductility.
 - d. an increase in gamma/gamma prime lattice mismatch which, based on a previous study, may lead to improved creep resistance at low to intermediate temperatures.
4. A corollary from 3 is that any compositional variation can have both beneficial and adverse consequences on creep and, therefore, should be made with care.
5. The stacking fault energy of a superalloy matrix is rather low and, therefore, the heterogeneous planar slip deformation characteristics was not changed in a major way by a variation of cobalt content.
6. An empirical equation has been proposed which can predict the stacking fault energy of nickel-base superalloy matrix accurately.

REFERENCES

1. O. H. Kriege and J. M. Baris: Trans. ASTM, 1969, Vol. 62, p. 195
2. J. M. Oblak and W. A. Owczarski: Trans. TMS-AIME, 1968, Vol. 242, p. 1563
3. J. W. Edington: Practical Electron Microscopy in Materials Science, p. 177, Van Nostrand Reinhold Co., NY, 1976
4. D. J. H. Cockayne, M. L. Jenkins and I. L. F. Ray: Phil Mag. 1971, p. 1383, 1971
5. J. B. Vander Sande: Introduction to Analytical Electron Microscopy, p. 535, Ed. J. M. Hren, J. I. Goldstein and D. C. Joy, Plenum, NY, 1979
6. C. B. Carter and S. M. Holmes: Phil. Mag., 1977, Vol. 35, p. 1161
7. C. H. Wells and C. P. Sullivan: Trans. ASM, 1964, Vol. 57, p. 841
8. H. Tada, P. C. Paris and G. R. Irwin: The Stress Analysis of Cracks Handbook, p. 2.1, Del Research Corp., Hellertown, PA, 1973
9. W. T. Read: Dislocations in Crystals, p. 131, McGraw-Hill, 1953
10. Y. T. Chou and J. D. Eshelby: J. Mech. Phys. Solids, 1962, Vol. 10, p. 27
11. F. Pfaff: Z. Metallkde, 1962, Vol. 53, p. 411
12. P. B. Hirsch, A. Howie, R. B. Nicholson, D. W. Pashley and M. J. Whelan: Electron Microscopy of Thin Crystals, p. 428, Plenum Press, NY, 1965
13. R. A. Mulford and U. F. Kocks: Acta Metall., 1979, Vol. 27, p. 1125
14. O. D. Sherby: Acta Metall., 1962, Vol. 10, p. 135
15. Diffusion Data, Vol. 6, No. 4, 1972, p. 570
16. J. I. Goldstein and H. Yakowitz: Practical Scanning Electron Microscopy, p. 204, Plenum Press, NY, 1975
17. R. D. Eng: Pratt and Whitney Aircraft, Private Communication, 1980
18. J. Heslop: Cobalt, 1964, No. 24, p. 128
19. C. C. Law and M. J. Blackburn: Met Trans. A, 1980, Vol 11A, p. 495

20. V. Sagar: PhD Thesis, Queen Mary College, London, 1971
21. A. M. Papon, J. P. Simon and G. Gugot: Phil. Mag. B, 1979, Vol. 39, O. 301
22. B. E. P. Beeston and L. K. France: J. Inst. Metals, 1968, Vol. 96, p. 105
23. J. M. Oblak: United Technologies Corp., Private Communication, 1976
24. G. E. Maurer, L. A. Jackman and J. A. Domingue: Proceedings of the Fourth International Symposium on Superalloys, J. K. Tien, S. T. Wlodek, H. Morrow III, M. Gell, and G. E. Maurer, eds., p. 43, ASM, Metals Park, OH 1980
25. A. Orlová and J. Čadek: Metal Science, 1981, January, p. 39
26. P. R. Strutt, R. S. Polvani, and B. H. Kear: Scripta Metall., 1973, Vol. 7, p. 949
27. M. J. Klein and M. E. Gulden: Metall. Trans., 1973, Vol. 4, p. 2175
28. R. L. Klueh and J. F. King: Metall. Trans. A, 1979, Vol. 10A, p. 1543
29. C. C. Law: Unpublished work, 1980
30. S. M. Copley and B. H. Kear: Trans. TMS-AIME, 1967, Vol. 239, p. 984
31. G. Chaland and L. Remy: Acta Metall., 1980, Vol. 28, p. 75
32. R. F. Decker: Symposium on Strengthening Mechanisms in Steels, Zurich, 1969, Climax Molybdenum Co., Greenwich, CT, 1970, p. 147

ACKNOWLEDGEMENTS

The authors would like to thank J. S. LeShane and V. S. Ajemian for their experimental assistance; K. Gumz and P. Genereux for characterization of powders by cathodoluminescence technique.

TABLE I
MATERIAL SOURCES

<u>Metal</u>	<u>Import Reliance (%)</u>	<u>Major Deposits</u>
Columbium	100	Brazil, Malaysia, Nigeria
Cobalt	97	Zaire, Zambia, Canada, Finland
Tantalum	97	Malaysia, Thailand, Australia
Chromium	89	Zimbabwe, S. Africa, USSR
Nickel	70	Canada, New Caledonia
Tungsten	38	China, Turkey
Titanium	38	Australia

TABLE II
PRATT & WHITNEY AIRCRAFT ALLOYS

<u>Alloy</u>	<u>Ni</u>	<u>Co</u>	<u>Cr</u>	<u>Al</u>	<u>Ti</u>	<u>Mo</u>	<u>Nb</u>	<u>Hf</u>
Waspaloy	58.6	13.5	19.5	1.4	3.0	4.0	-	-
Astroloy	55.5	17.0	15.0	4.0	3.5	5.0	-	-
IN 100	56.7	18.5	12.5	5.0	4.3	3.0	-	-
MERL 76	54.8	18.5	12.5	5.0	4.3	3.0	1.6	0.3

TABLE III
COMPOSITIONS OF MERL 76 AND ITS MATRIX PHASE (WEIGHT %)

	Ni	Cr	Co	Al	Ti	Mo	Hf	Nb	B	Zr	C
MERL 76	55.5	12.2	18.3	5.1	3.9	3.2	0.37	1.37	0.024	0.05	0.01
Matrix (54%v')	39.5	23.5	27.9	2.37	1.19	4.99	0.12	0.43	-	-	-
Matrix (60%v')	35.3	26.5	30.4	1.66	0.07	5.45	0.06	0.18	-	-	-

TABLE IV
COMPOSITIONS OF GAMMA ALLOYS (WEIGHT %)

Alloy	Ni	Cr	Co	Al	Ti	Mo	Hf	Nb
29	36.5	25.9	30.6	0.70	0.53	5.0	0.14	0.44
30	50.3	26.0	16.7	0.62	0.50	5.1	0.10	0.42
31	58.8	26.0	7.6	0.65	0.61	5.4	0.11	0.44
32	66.0	26.1	0.0	0.55	0.62	5.5	0.10	0.54

TABLE V
HOT ISOSTATIC PRESSING* (HIP) AND SOLUTION TREATMENT* TEMPERATURES

Alloy	HIP, °C	Solution, °C
18% Co MERL 76	1180	1170
10% Co MERL 76	1205	1195
0% Co MERL 76	1220	1205
15% Co AF115	1160	1175
10% Co AF115	1200	1185
0% Co AF115	1220	1205

*HIP at the indicated temperature for 3 h at 100 MPa.
Solution treatment at the indicated temperature for 2h
followed by air cooling.

TABLE VI
ALLOY COMPOSITIONS (WEIGHT %)

	<u>18% Co</u> <u>MERL 76</u>	<u>10% Co</u> <u>MERL 76</u>	<u>0% Co</u> <u>MERL 76</u>	<u>15% Co</u> <u>AF115</u>	<u>10% Co</u> <u>AF115</u>	<u>0% Co</u> <u>AF115</u>
Ni	Bal.	Bal.	Bal.	Bal.	Bal.	Bal.
Co	18.6	9.7	-	15.0	10.00	-
Cr	11.8	12.0	12.3	10.5	10.7	10.8
Mo	3.2	3.3	3.0	2.8	2.8	2.9
W	-	-	-	6.0	5.9	5.7
Al	4.9	5.0	4.8	3.9	3.8	3.8
Ti	4.3	4.0	4.0	3.9	3.9	4.0
Nb	1.30	1.20	1.21	1.80	1.70	1.64
Hf	0.43	0.43	0.38	2.10	0.75	0.83
B	0.019	0.020	0.017	0.020	0.020	0.021
Zr	0.080	0.055	0.047	0.050	0.050	0.060
C	0.020	0.011	0.022	0.150	0.050	0.055

TABLE VII

EQUILIBRIUM SEPARATIONS OF PARTIAL DISLOCATIONS IN
GAMMA ALLOYS AND CALCULATED STACKING FAULT ENERGIES

Alloy	Cobalt (At. %)	Avg. Separation of Partials (nm)	Stacking Fault Energy, Γ		
			Isotropic Γ (mJm ⁻²)	$\Gamma/Gb(10^{-3})$	Anisotropic _{c₂} Γ (mJm ⁻²)
29	29.9	11.7	18.8	0.78	15.0
30	16.3	7.7	28.1	1.18	22.5
31	7.4	-	33.5*	1.42*	-
32	0.0	5.6	37.9	1.62	30.6

*Interpolated Value

TABLE VIII

YIELD STRENGTHS AND MINIMUM CREEP RATES OF GAMMA ALLOYS
AT 704°C/1.2 x YIELD STRENGTH

Alloy	Wt.% of Cobalt	0.2% Y.S. (MPa)	Creep Rate (x10 ⁻⁵) (h ⁻¹)
29	30.6	160.5	1.5
30	16.7	149.5	10.5
31	7.6	136.4	12.5
32	0.0	130.9	33.4

TABLE IX
CREEP RUPTURE PROPERTIES OF MERL 76 BASE ALLOYS AT 704°C

Cobalt Content Wt. %	Stress MPa	Elong. %	RA %	Life h
18	550	2.1	5.8	864.6
10	550	3.5	11.5	1635.3
0	550	3.2	1.9	36.1
18	655	5.3	10.1	497.9
10	655	3.8	16.0	405.6
0	655	2.7	1.6	10.0
18	760	8.0	25.4	180.0
10	760	9.4	14.4	200.0
0	760	1.9	1.0	2.6
18	860	9.9	10.7	43.0
10	860	9.9	15.4	40.4
0	860	3.8	2.4	1.5

TABLE X
CREEP RUPTURE PROPERTIES OF AF115 BASE ALLOYS AT 704°C

Cobalt Content Wt. %	Stress MPa	Elong. %	RA %	Life h
0	550	1.7	1.0	77.2
10	550	-	-	750.0+
0	650	1.9	1.6	32.9
10	650	2.7	1.7	458.7
15	690	6.0	2.8	641.7
15	760	4.6	4.5	495.3
10	760	1.9	1.8	358.9
0	760	1.4	2.3	6.5
15	860	3.3	5.9	66.9
10	860	5.2	6.6	69.0
0	860	2.4	2.3	2.1

+ No failure, test discontinued

TABLE XI
FATIGUE FRACTURE LIVES OF MERL 76
BASE ALLOYS AT 480°C and 650°C
Total Strain Range 0.014, $R_e = -1$, 10 Cycles Per Min.

Cobalt Content Wt. %	480°C Cycles	650°C Cycles
18	1537	610
10	328	357
0	234	122

TABLE XII
STACKING FAULT COEFFICIENTS A_i FOR NICKEL SOLID SOLUTIONS

Element	Al	Ti	Cr	Fe	Co	Mo	W
A_i	0.019	0.085	0.028	0.007	0.016	0.066	0.066

TABLE XIII
CALCULATED AND EXPERIMENTAL VALUES OF STACKING FAULT ENERGY

Alloy	Composition in Atomic %							$\Gamma / Gb, 10^{-3}$	
								Calc. Eq. 6	Expt.
	Ni	Cr	Co	Mo	W	Al	Ti		
29	36.0	28.7	29.9	3.0	-	1.49	0.64	1.08	0.78
30	49.6	28.8	16.3	3.1	-	1.32	0.60	1.35	1.18
31	58.1	28.8	7.4	3.2	-	1.39	0.73	1.55	1.42
32	65.4	29.0	0.0	3.3	-	1.18	0.75	1.75	1.62
* Waspaloy	Bal.	25.0	16.1	3.2	-	1.10	0.73	1.53	1.49(22)
* Mar-M200	Bal.	20.4	13.4	-	4.0	3.20	-	1.76	1.75(22)

* Matrix compositions

TABLE XIV

SUMMARY OF EFFECTS OF DECREASING COBALT CONTENT
ON MICROSTRUCTURE AND CREEP PROPERTIES OF MERL 76

<u>Microstructure</u>	<u>Creep*</u>
<u>Increase SFE</u>	-
<u>Increase solubility of Al and Ti in γ</u>	
Decrease precipitation of fine γ' particles	-
Decrease SFE	+
<u>Decrease solubility of C in γ</u>	
Increase precipitation of Cr-Mo rich carbide	Reduces Ductility
Increase SFE	-
Increase γ/γ' lattice misfit	+
* - reduces creep resistance	
+ increases creep resistance	

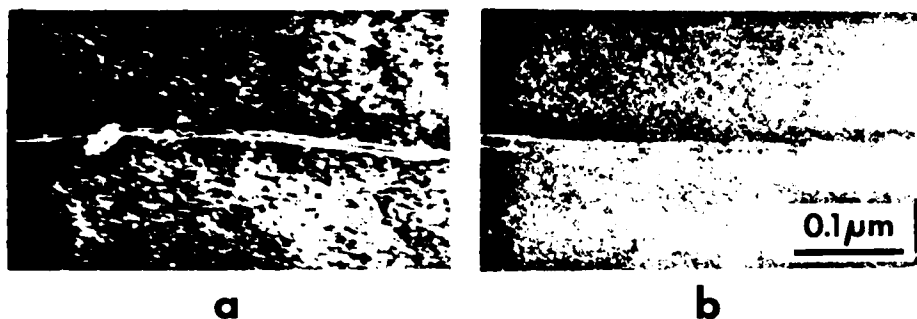


Fig. 1 Separation of Shockley partials imaged by weak beam dark field technique \bar{g} ($3\bar{g}$), $\bar{g} = 022$. a. Alloy 32 (0% Co) b. Alloy 29 (30% Co)

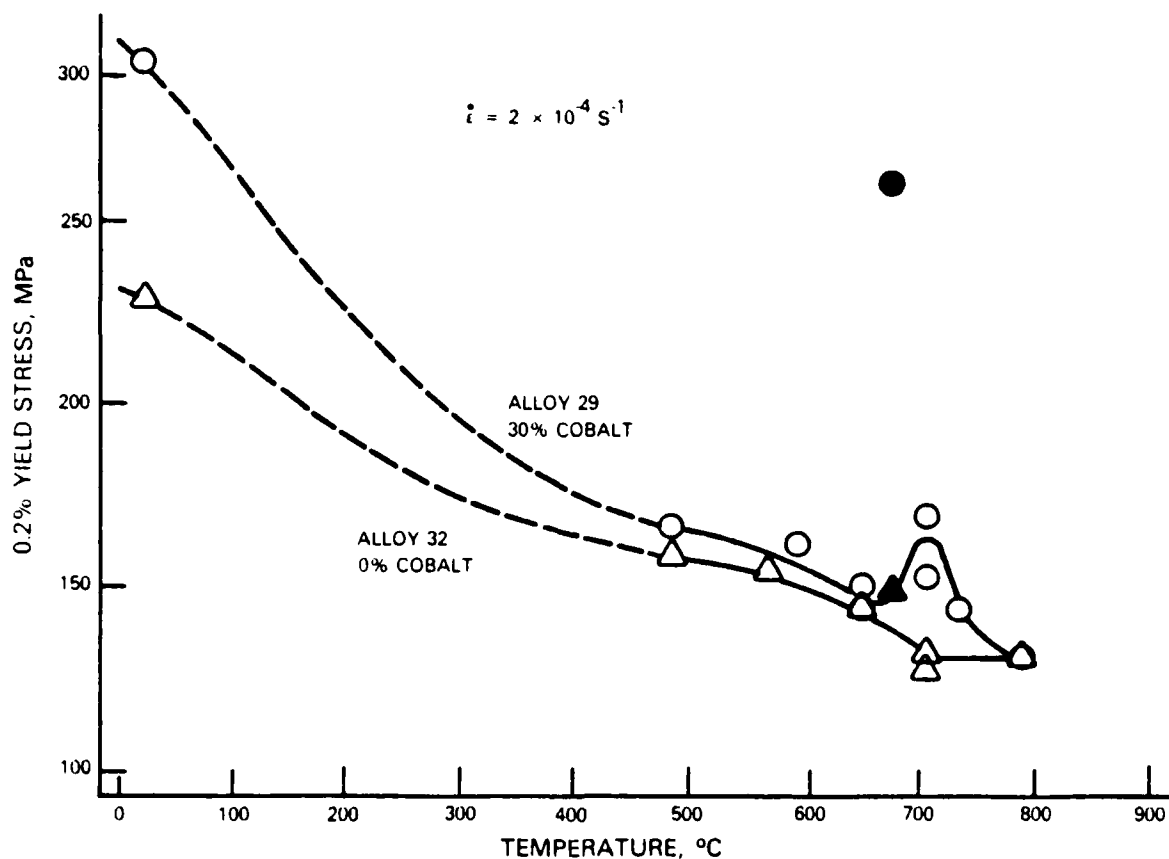


Fig. 2 0.2% yield strengths of Alloys 29 (30 wt.% cobalt) and 32 (0 wt.% cobalt) vs temperature. The yield strengths after aging for 90 h at the test temperature are given by the filled data points

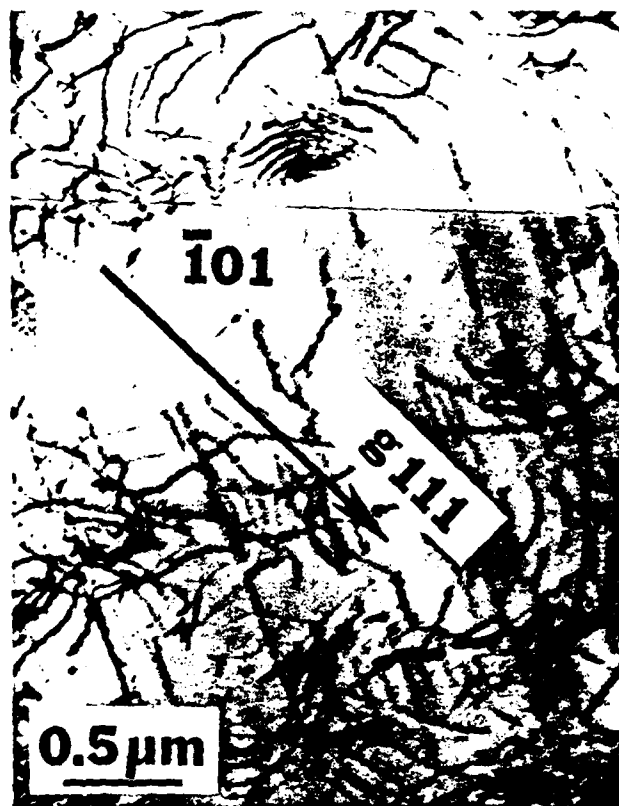


Fig. 3 Dislocation structure in an Alloy 32 sample yielded at 704°C to a strain of 0.037

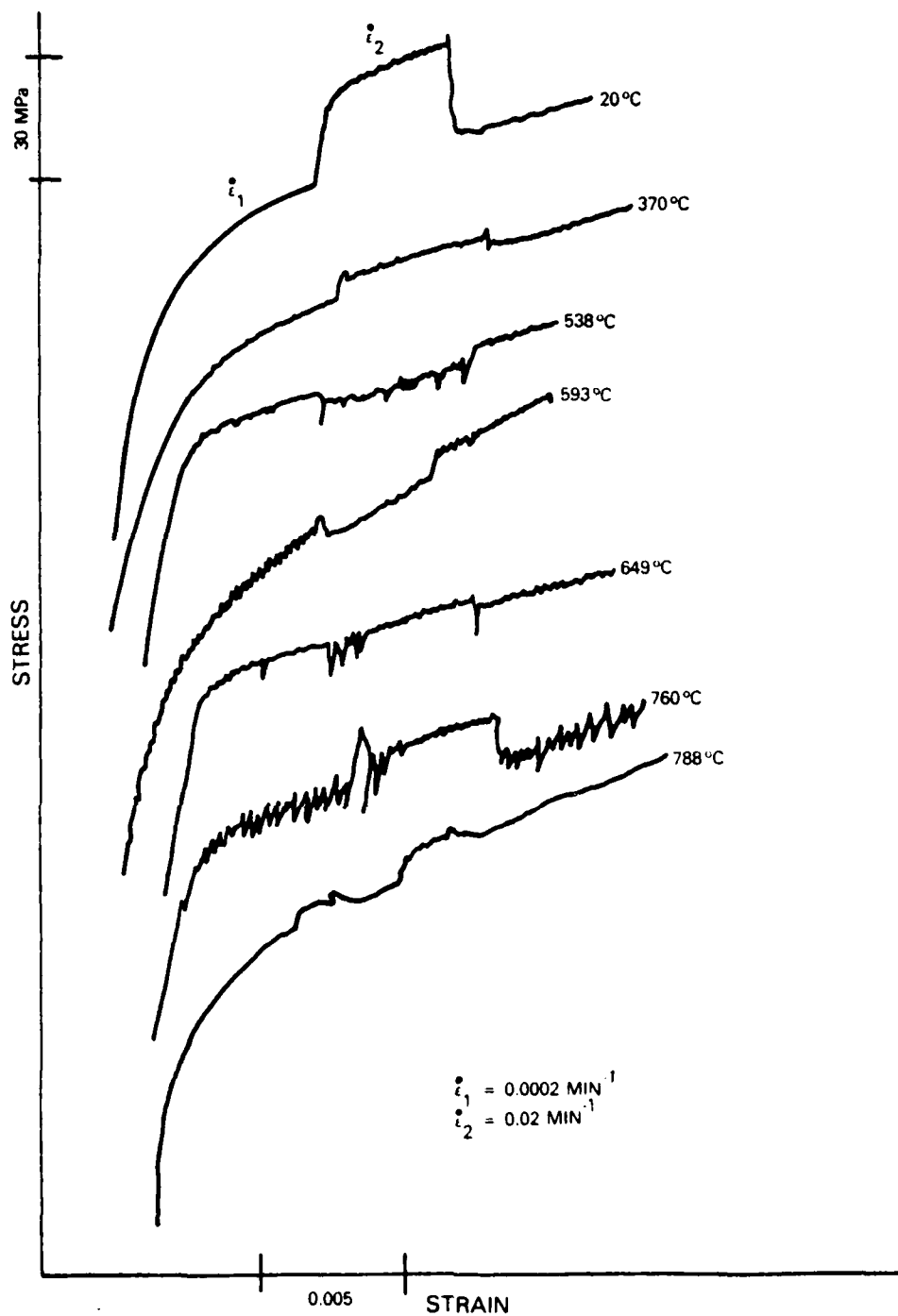


Fig. 4 Jerky flow and stress sensitivity of strain rate in Alloy 29

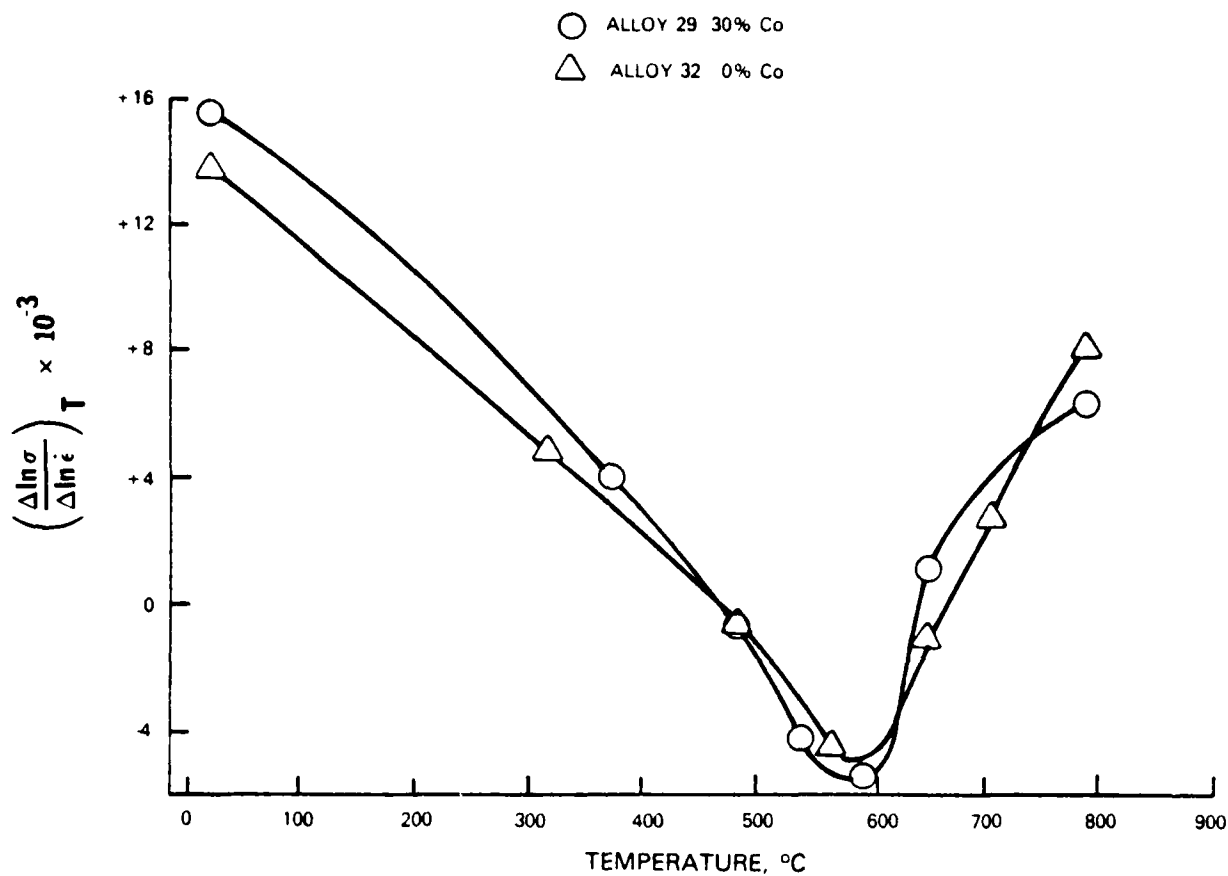


Fig. 5 Strain rate sensitivity in Alloys 29 and 32

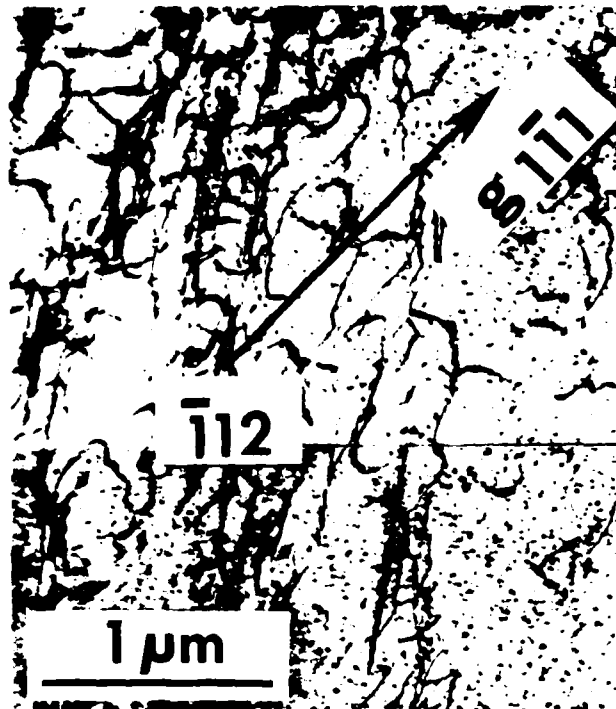


Fig. 6 Dislocation structure in an Alloy 29 sample creep tested at 704°C, 195 MPa to a strain of 0.024

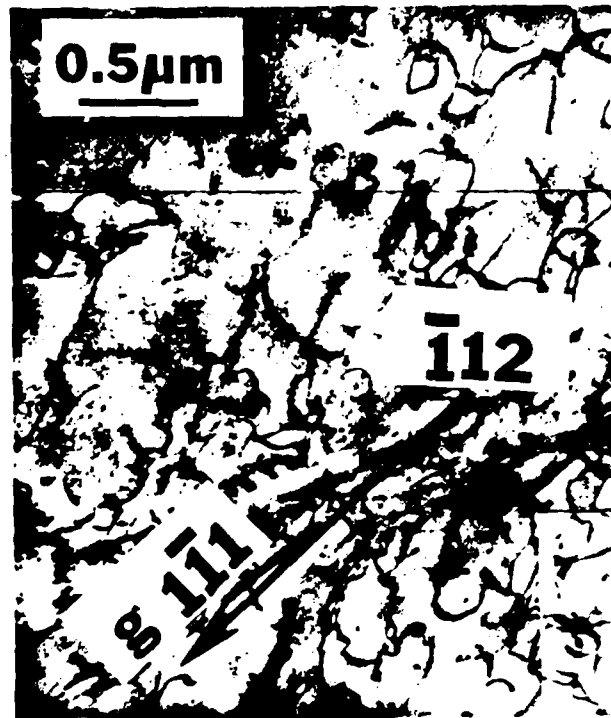


Fig. 7 Dislocation structure in an Alloy 32 sample creep tested at 704°C, 160 MPa to a strain of 0.030

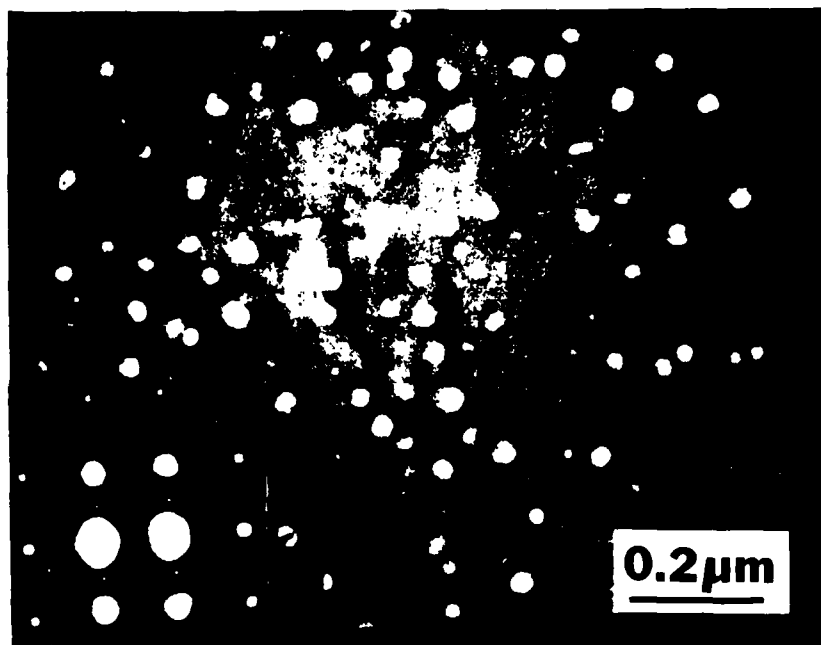


Fig. 8 Dark field electron micrograph of the fine gamma prime particles in an Alloy 29 sample creep tested at 704°C, 195 MPa. Insert shows the superlattice diffraction spots from the fine gamma prime particles



Fig. 9 Dislocation loops surrounding the fine gamma prime particles in an Alloy 29 sample creep tested at 704°C, 195 MPa

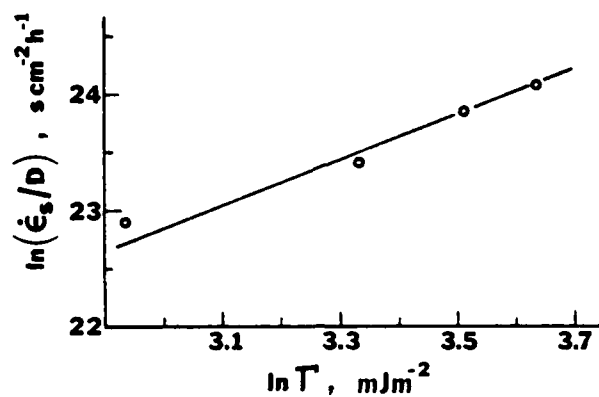


Fig. 10 $\ln(\dot{\epsilon}_s/D)$ versus $\ln T$ for the gamma alloys at 800°C and (σ/E) of 5.3×10^{-4}

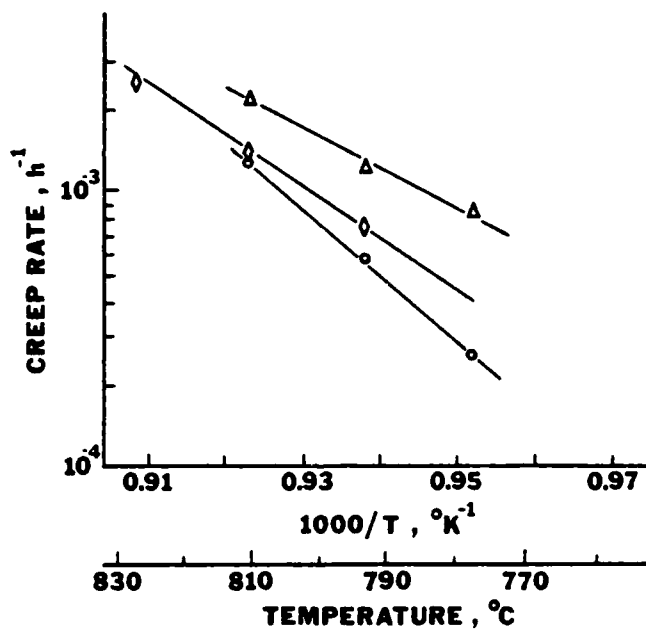


Fig. 11 Creep rate versus temperature for Alloy 29 (30% Co), Alloy 30 (17% Co), and Alloy 32 (0% Co) at a stress of 110 MPa

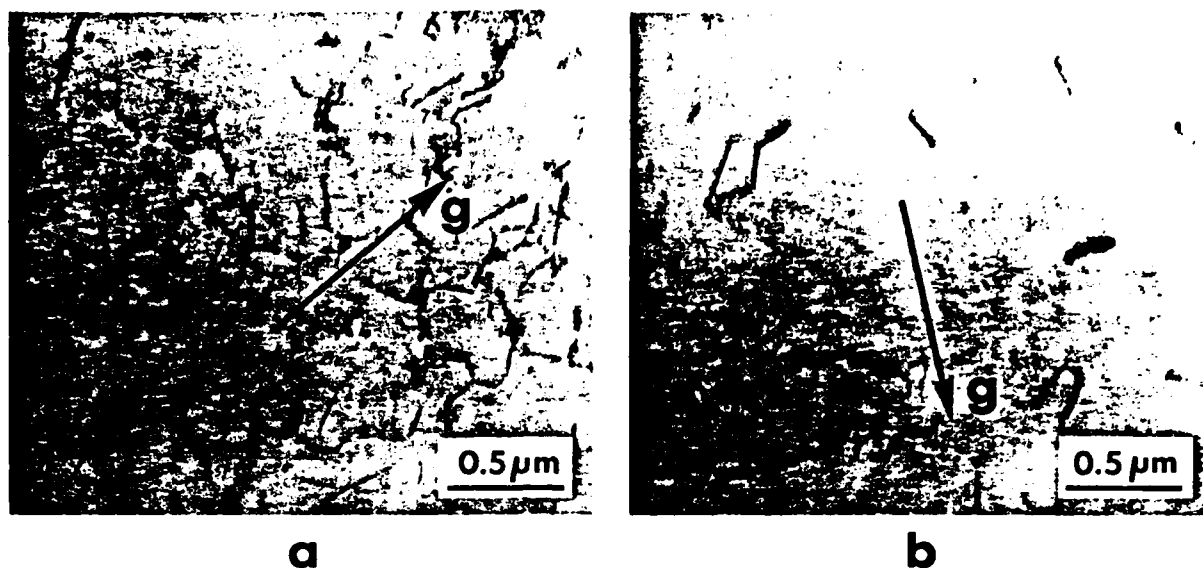


Fig. 12 Dislocation structures after creep testing at 800°C/110 MPa, plane of observation (011), $\vec{g} = \langle 11\bar{1} \rangle$ a. Alloy 29 (30% Co) at a creep strain of 0.025, dislocation density = $1.3 \times 10^{10} \text{cm}^{-2}$. b. Alloy 32 (0% Co) at a creep strain of 0.044, dislocation density = $3.2 \times 10^9 \text{cm}^{-2}$

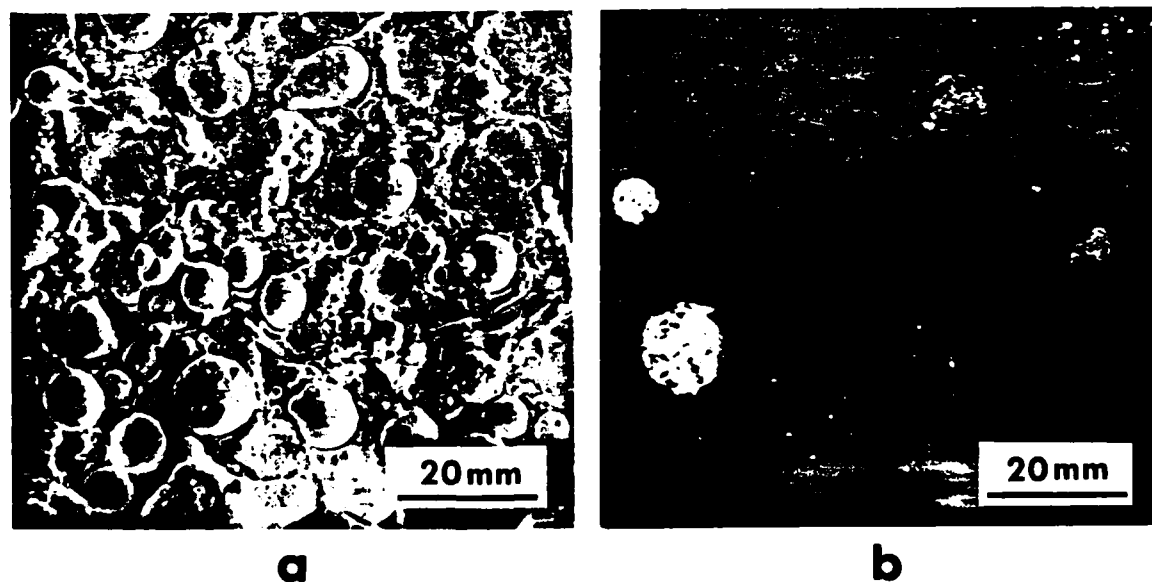


Fig. 13 a. 10% Co AF115 powder particles revealed by cathodoluminescence b. Oxide-covered powder particles

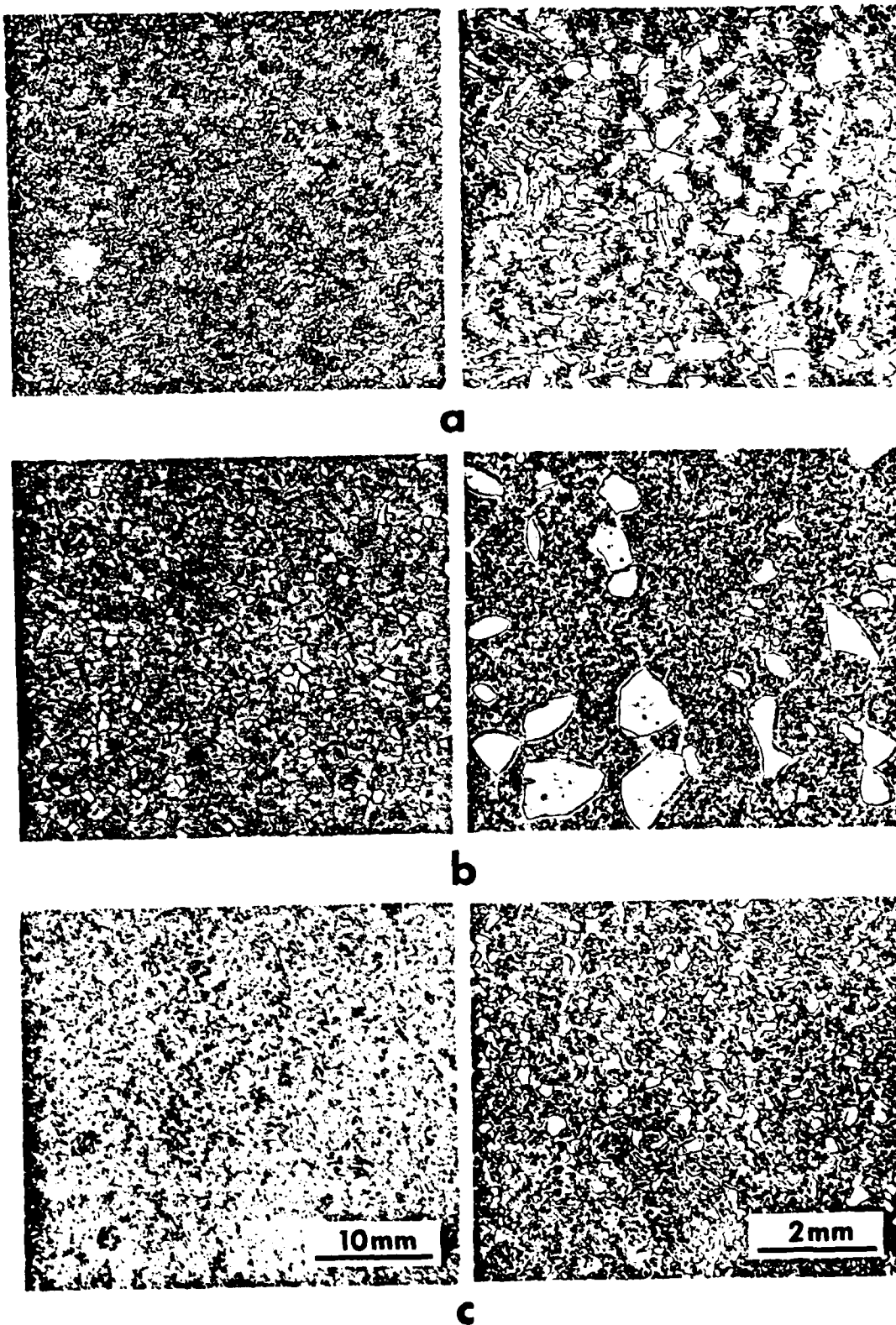


Fig. 14 Microstructures of a. 0% Co MERL 76 b. 10% Co MERL 76 c. 18% Co MERL 76, all after heat treatments given in Table V

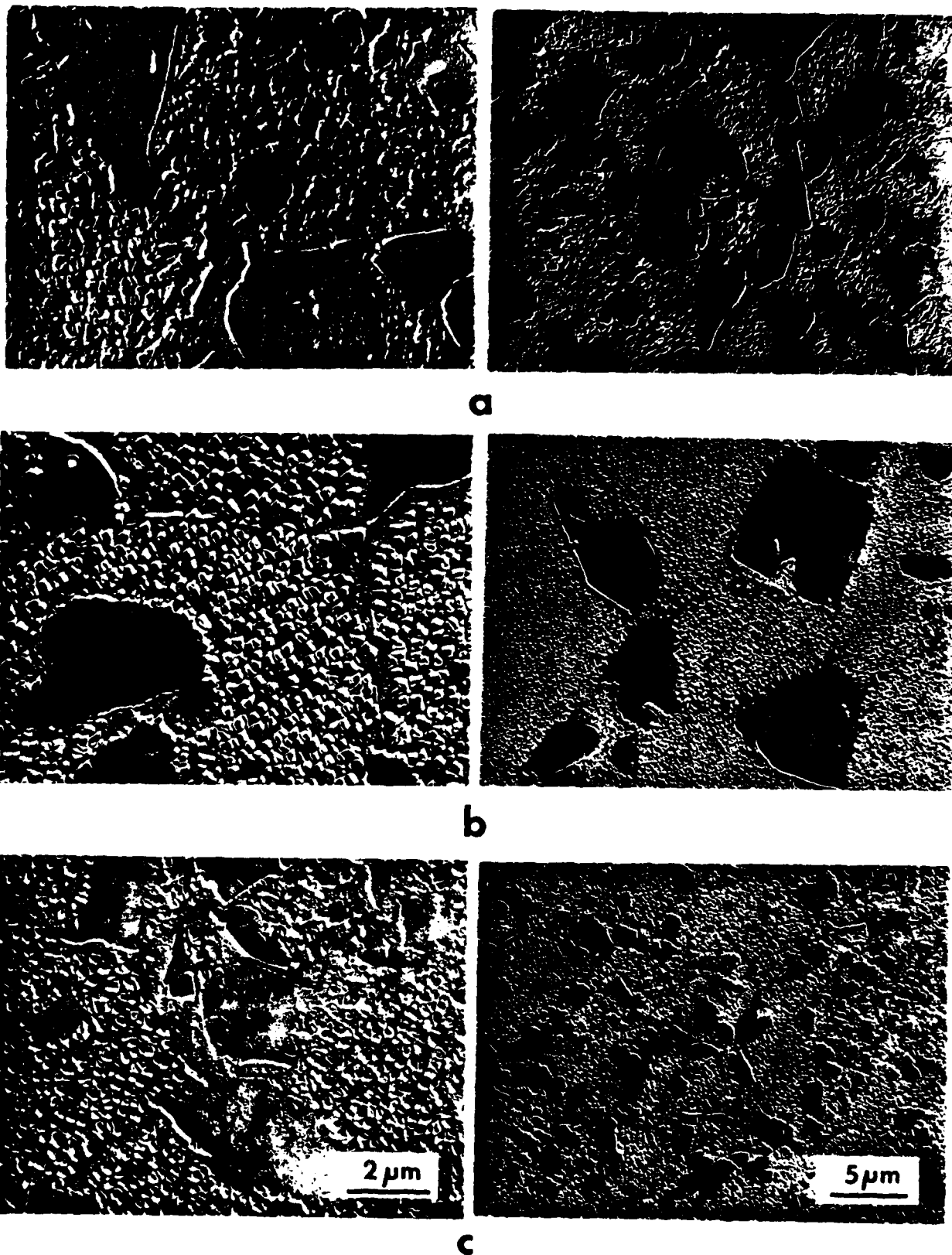


Fig. 15 Microstructures of a. 0% Co MERL 76 b. 10% Co MERL 76 c. 18% Co MERL 76, all after heat treatments given in Table V

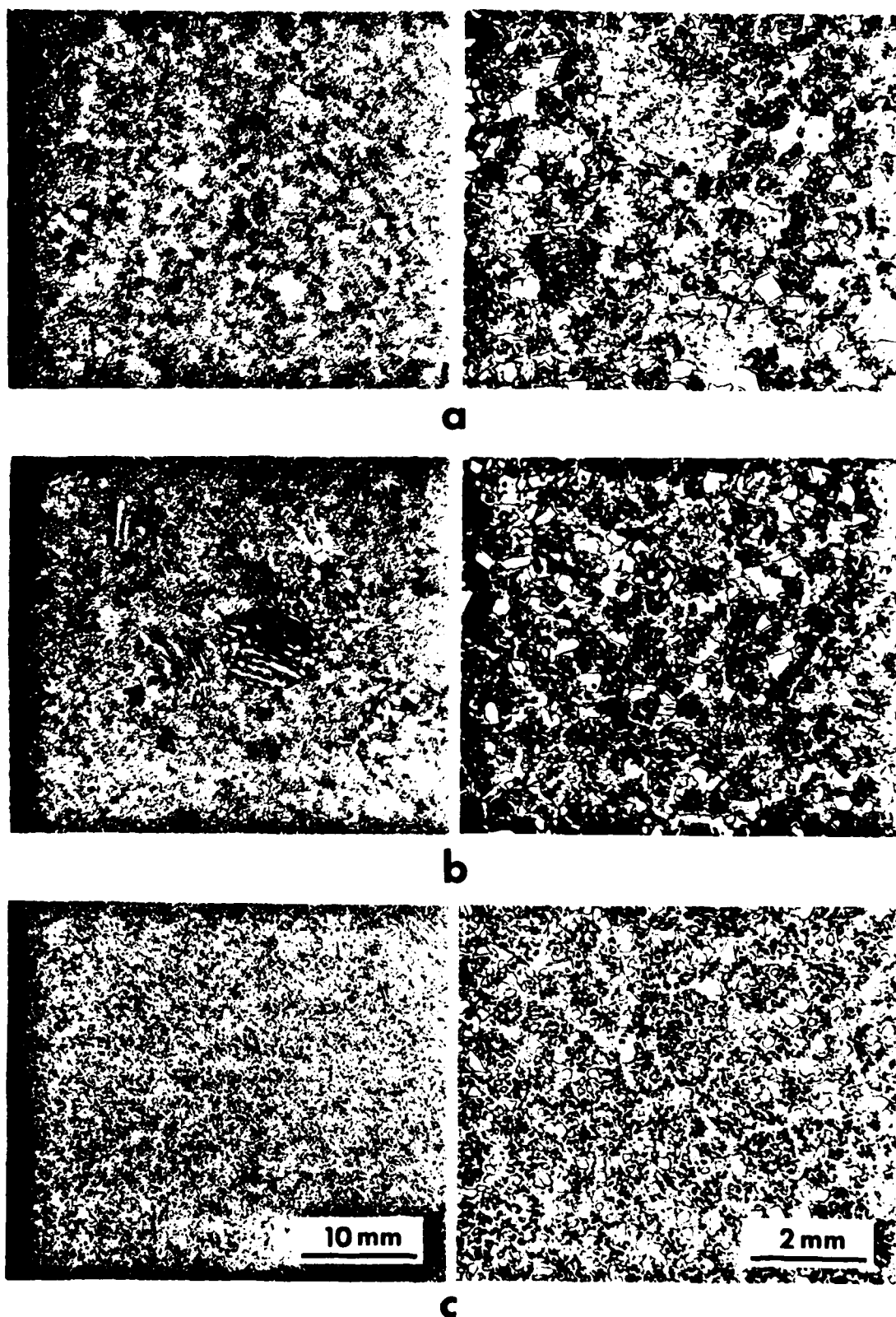


Fig. 16 Microstructures of a. 0% Co AF115 b. 10% Co AF115 c. 15% Co AF115, all after heat treatments given in Table V



a

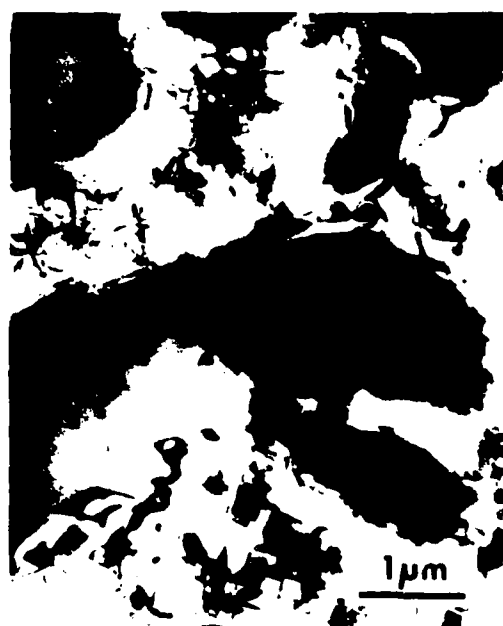


b

Fig. 17 Microstructures of a. 18% Co MERL 76 b. 0% Co MERL 76. Note the precipitation of γ particles (small dark spots) within the secondary γ' particles in both alloys



a



b

Fig. 18 Grain boundary microstructures of a. 18% Co MERL 76 b. 0% Co MERL 76

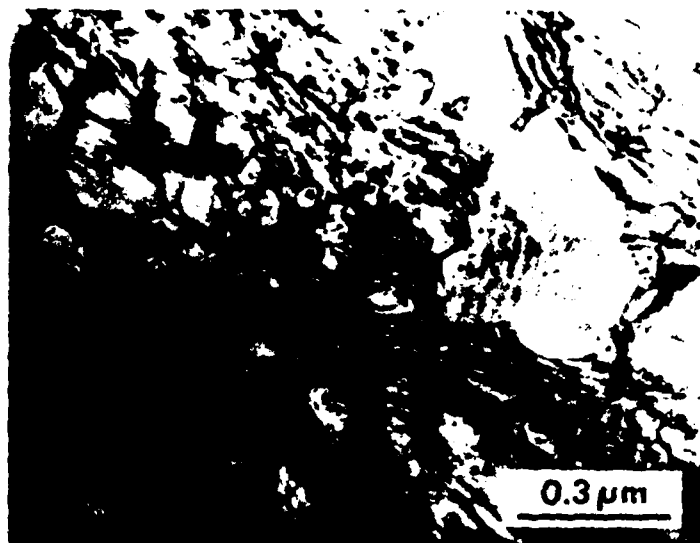


Fig. 19 Fringe contrast at the v/v' interface of the 0% Co MERL 76, $\bar{g} = 111$

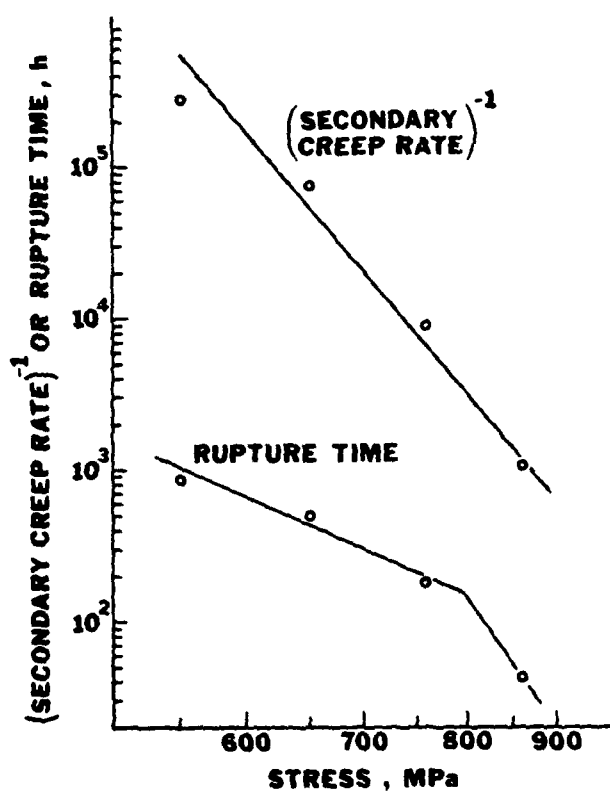


Fig. 20 Creep-rupture life, secondary creep rate versus stress for the 18% Co MERL 76 at 704°C

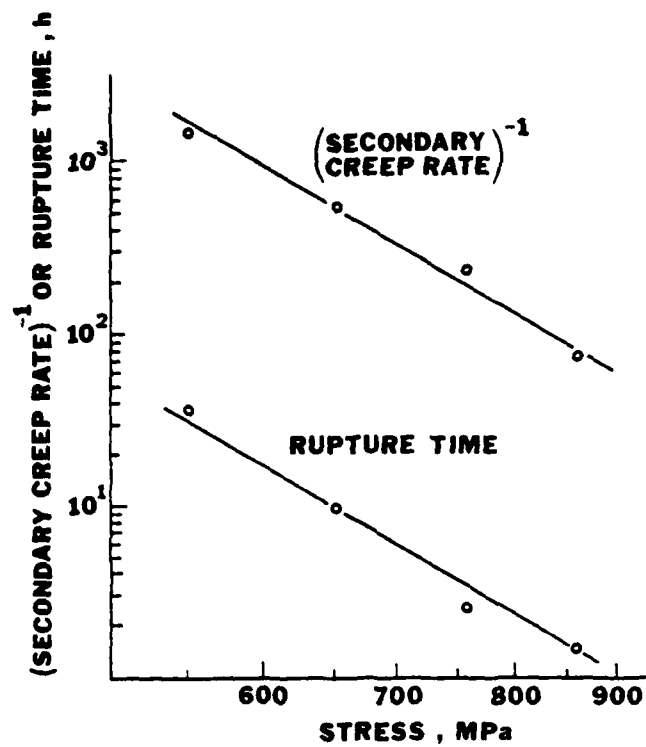


Fig. 21 Creep-rupture life, secondary creep rate versus stress for the 0% Co MERL 76 at 704°C

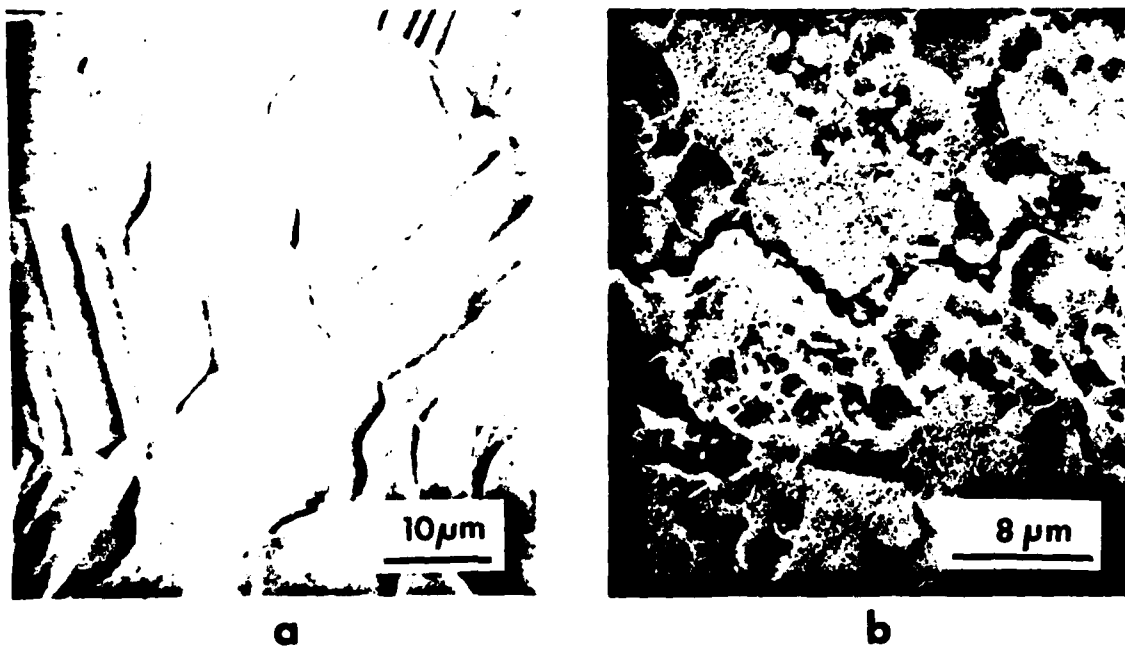


Fig. 22 Creep fractures surfaces at 704°C a. 18% Co MERL 76 at 650 MPa (Ref.19) b. 0% Co MERL 76 at 550 MPa

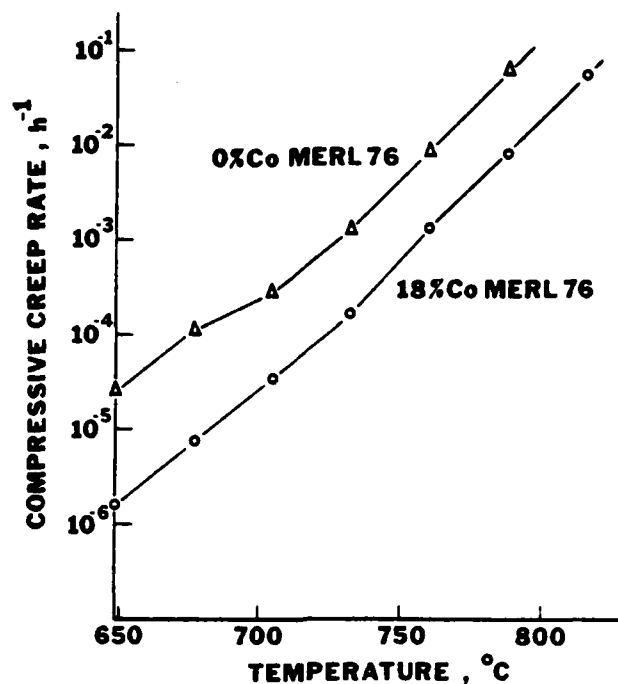


Fig. 23 Compressive creep rate versus temperature for the 18% Co MERL 76 and 0% Co MERL 76 under a stress of 860 MPa

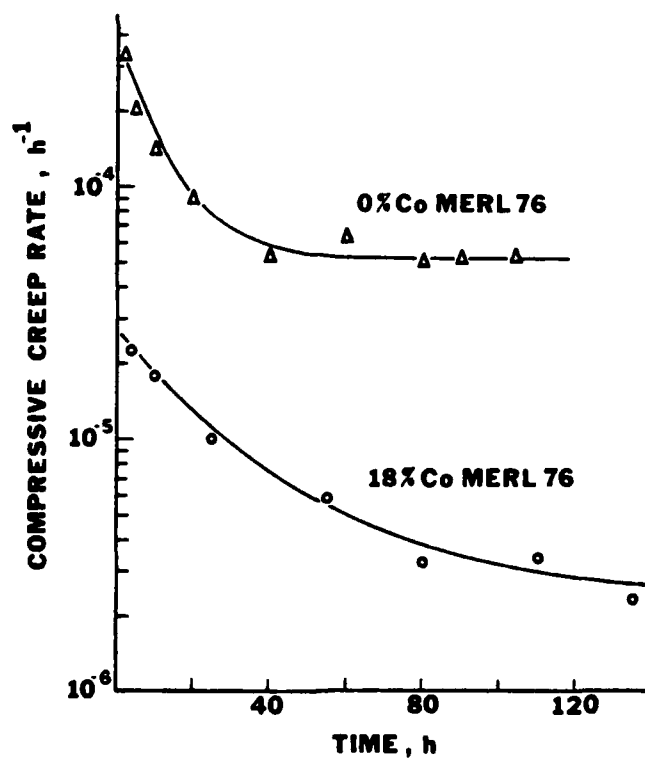


Fig. 25 Compressive creep rate versus time for the 18% Co MERL 76 and 0% Co MERL 76 at 675°C, 860 MPa

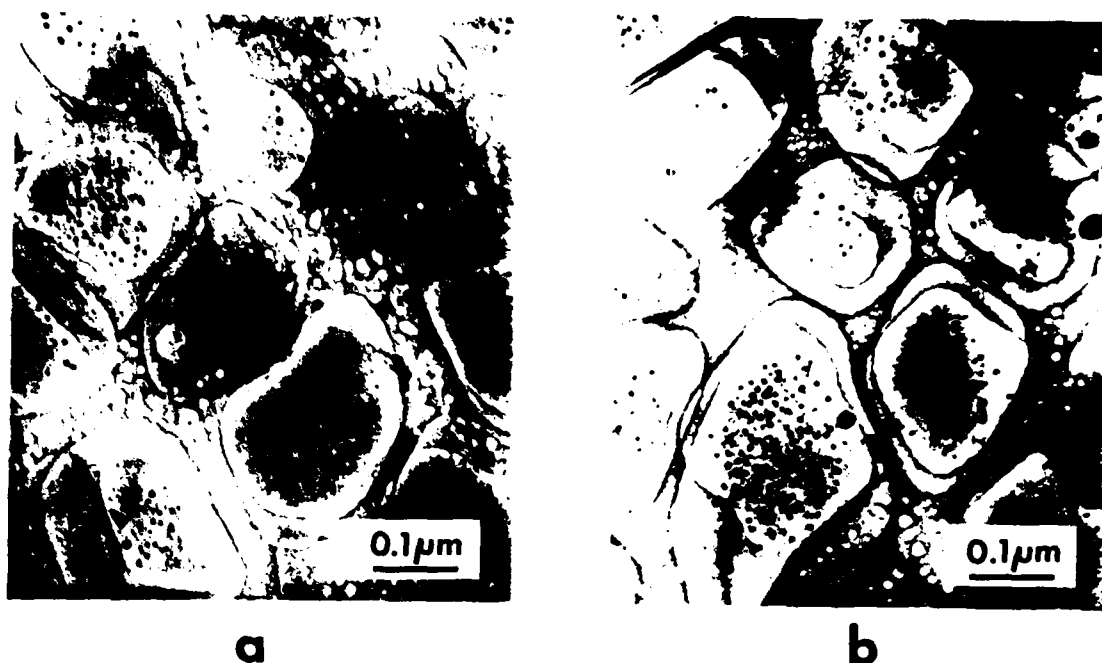


Fig. 24 Precipitation of very fine v' particles in 18% Co MERL 76 a. After creep test for 130h at 675°C b. As heat-treated. Note the precipitation of v particles (small dark spots) within the secondary v' particles



Fig. 26 Intragranular precipitation of Cr-Mo rich carbide platelets in the 0% Co MERL 76 after creep testing at 675°C for 100h

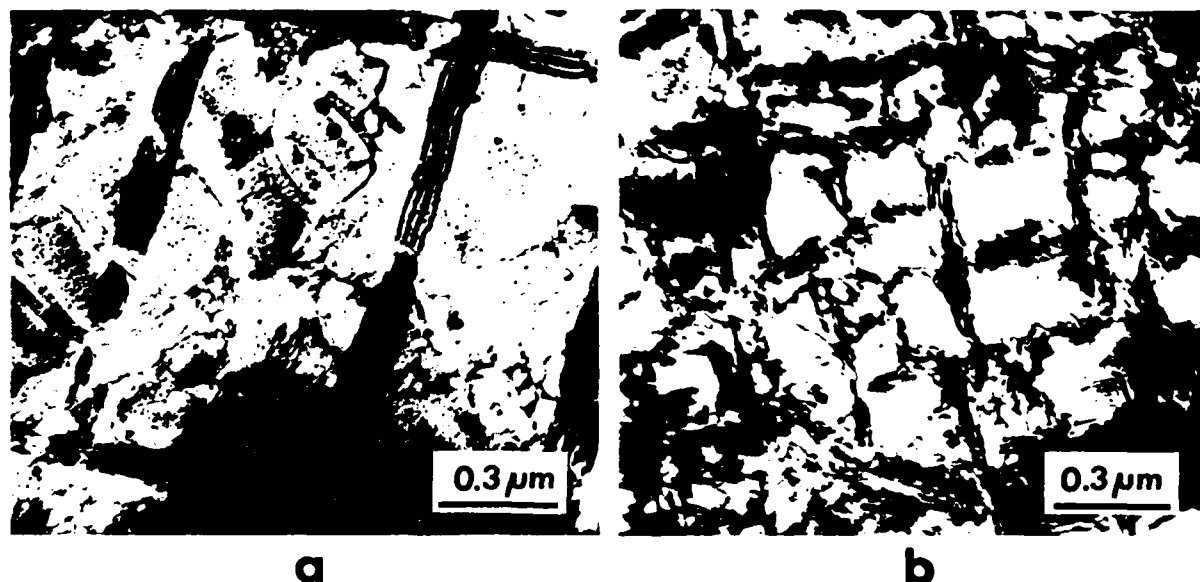


Fig. 27 Dislocation structures after creep testing at 704°C, 860 MPa
 a. 18% Co MERL 76 at a strain of 0.006 b. 0% Co MERL 76 at a strain of 0.013

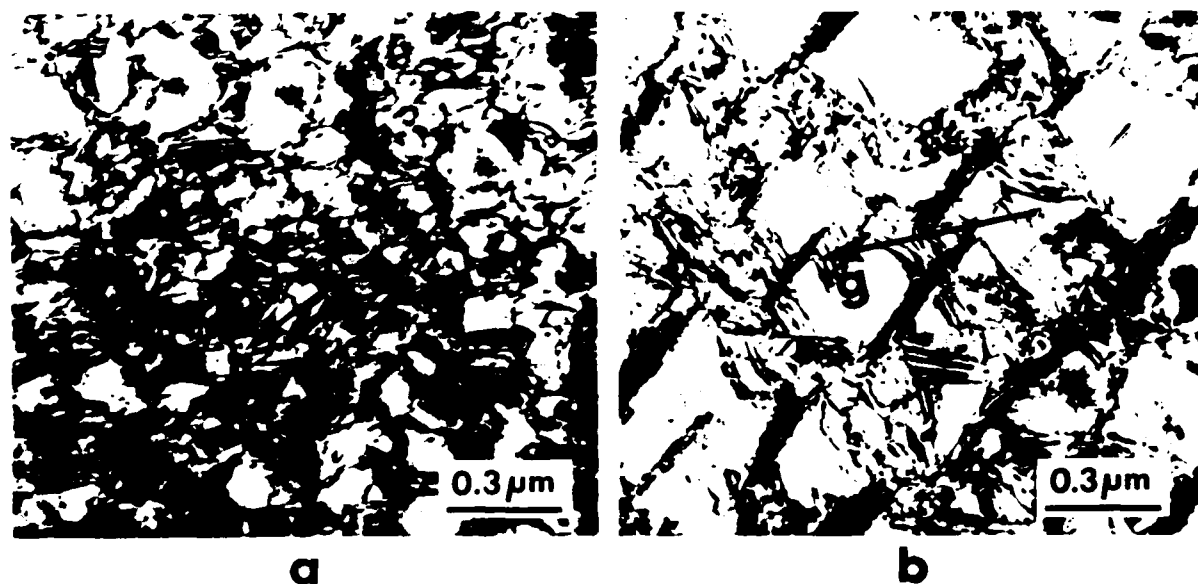
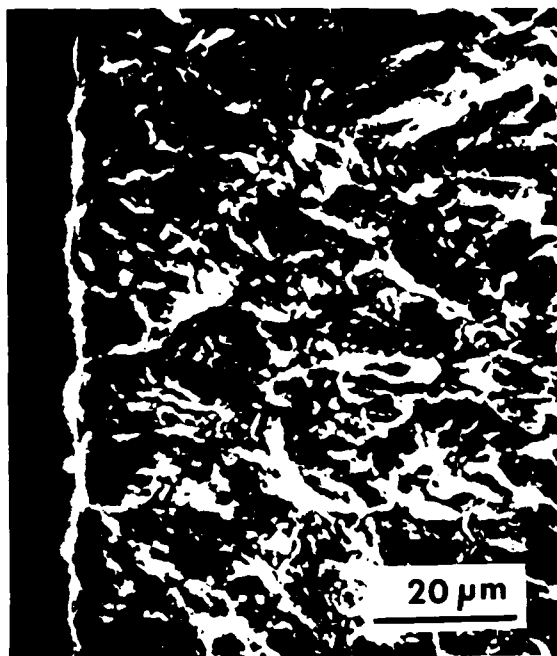
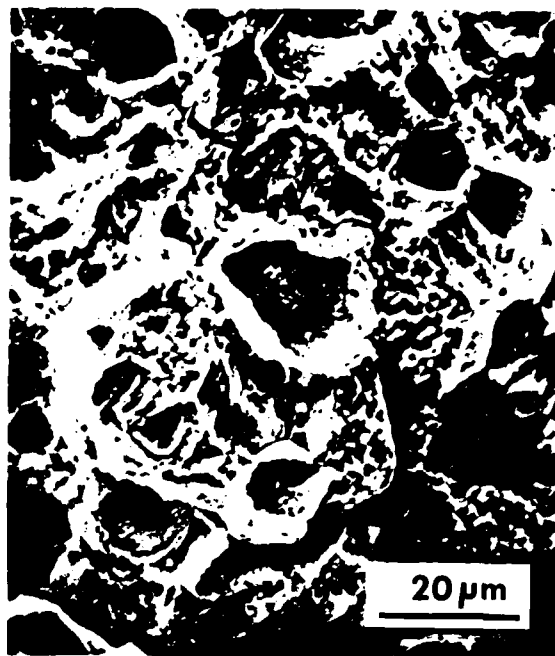


Fig. 28 Dislocation structures after creep testing at 815°C, 690 MPa to a strain of 0.017 a. 18% Co MERL 76, $\bar{g} = 11\bar{1}$ b. 0% Co MERL 76, note the fringe contrast at the γ/γ' interface. $\bar{g} = 11\bar{1}$



a



b

Fig. 29 Fatigue fracture at 650°C, total strain range of 0.014, $R = -1$, 10 cycles per minute a. 18% Co MERL 76 b. 0% Co MERL 76

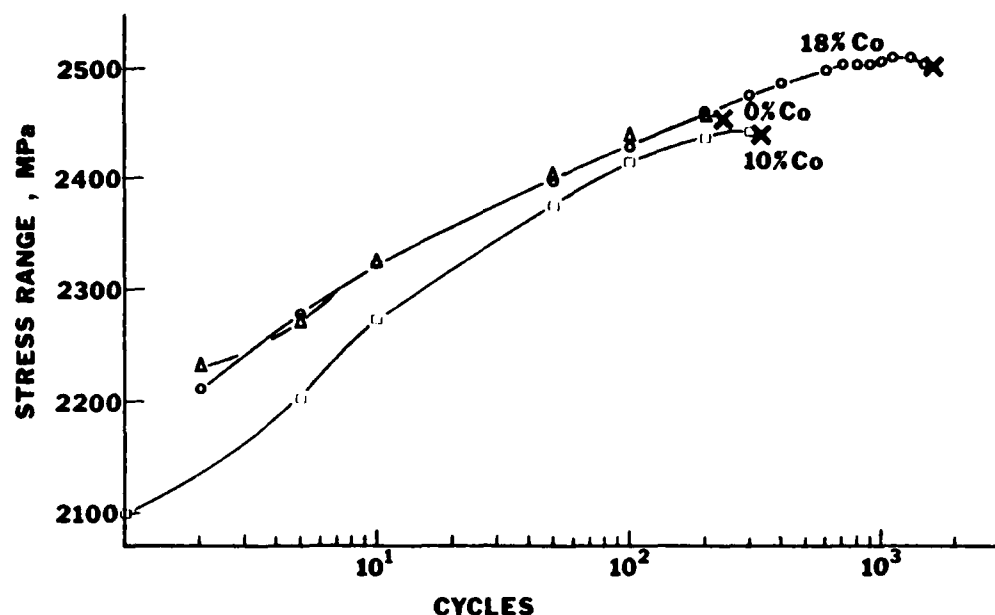


Fig. 30 Stress range versus strain cycles for MERL 76 base alloys containing 18% Co, 10% Co, and 0% Co tested at 480°C, total strain range of 0.014, $R = -1$, 10 cycles per minute

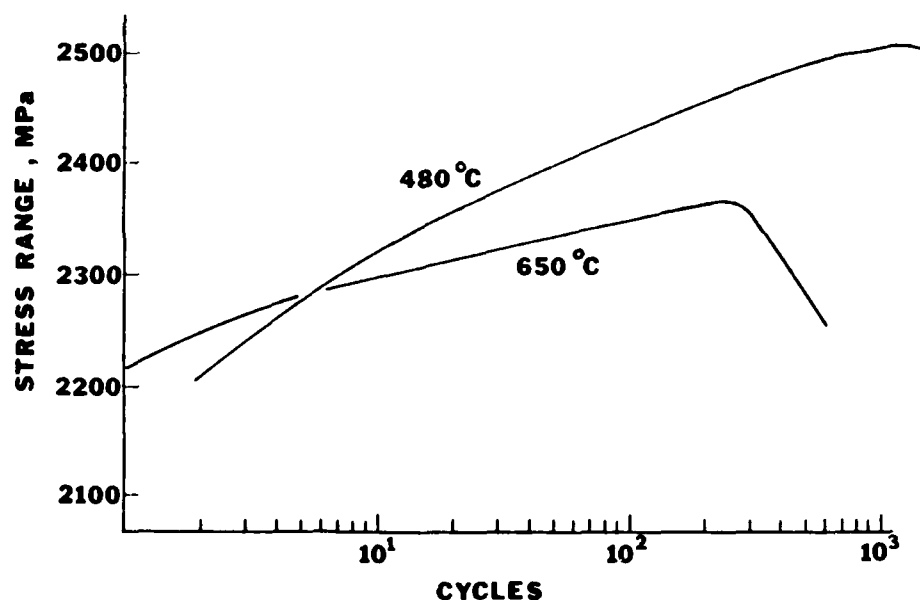


Fig. 31 Stress range versus strain cycles for 18% Co MERL 76 tested at 480°C and 650°C, total strain range of 0.014, $R = -1$, 10 cycles per minute



Fig. 32 Dislocation structure of the 0% Co MERL 76 at an early stage of fatigue testing at 650°C, total strain range of 0.014, $R = -1$, 10 cycles per minute

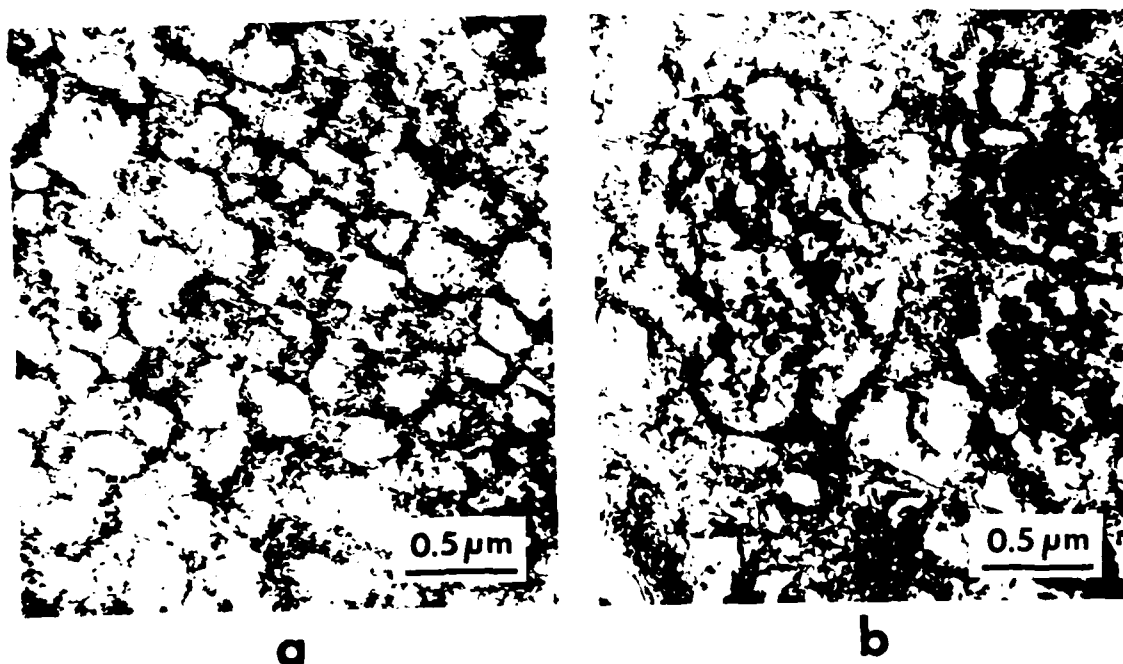


Fig. 33 Dislocation structures in a. 18% Co MERL 76 and b. 0% Co MERL 76, after fatigue testing to fracture at 650°C, total strain range of 0.014, $R = -1$, 10 cycles per minute

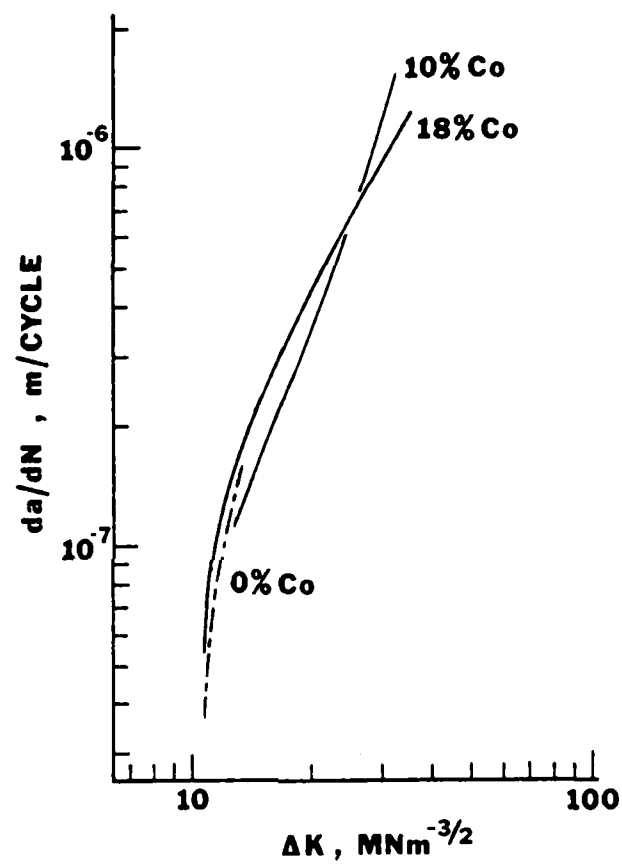


Fig. 34 da/dN versus ΔK for MERL 76 base alloys containing 0%, 10%, and 18% Co

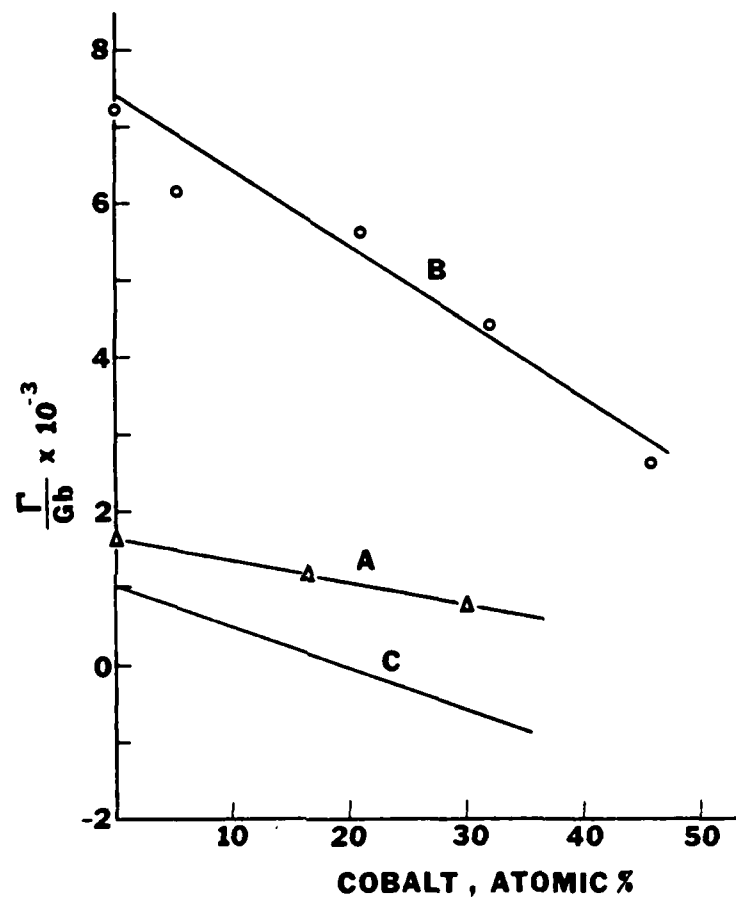


Fig. 35 Stacking fault energy versus cobalt content a. Experimental data of gamma alloys b. Experimental data of Ni-Co binary alloys from Ref. 20 c. Calculated values for the gamma alloys using Eqn. 6

DAI
FILM